

# Emerging Multifunctional Nanostructures

Guest Editors: Hongyou Fan, Yunfeng Lu,  
Ganapathiraman Ramanath, and José A. Pomposo





---

# **Emerging Multifunctional Nanostructures**

Journal of Nanomaterials

---

## **Emerging Multifunctional Nanostructures**

Guest Editors: Hongyou Fan, Yunfeng Lu,  
Ganapathiraman Ramanath, and Jos A. Pomposo



---

Copyright © 2008 Hindawi Publishing Corporation. All rights reserved.

This is a special issue published in volume 2008 of “Journal of Nanomaterials.” All articles are open access articles distributed under the Creative Commons Attribution License, which permits unrestricted use, distribution, and reproduction in any medium, provided the original work is properly cited.

## Editor-in-Chief

Michael Z. Hu, Oak Ridge National Laboratory, USA

## Advisory Board

Taeghwan Hyeon, Korea  
James H. Adair, USA  
C. Jeffrey Brinker, USA  
Nathan Lewis, USA

Ed Ma, USA  
Alon V. McCormick, USA  
Gary L. Messing, USA  
Zhonglin Wang, USA

Enge Wang, China  
N. Xu, China  
Jackie Ying, USA

## Associate Editors

Alan K. T. Lau, Hong Kong  
Xuedong Bai, China  
Donald A. Bansleben, USA  
John Bartlett, Australia  
Theodorian Borca-Tasciuc, USA  
Christian Brosseau, France  
Siu Wai Chan, USA  
Sang-Hee Cho, South Korea  
Chun Xiang Cui, China  
Ali Eftekhari, Iran  
Claude Estournes, France  
Alan Fuchs, USA  
Lian Gao, China  
Hongcheng Gu, China  
Michael Harris, USA

Justin Holmes, Ireland  
David Hui, USA  
Wanqin Jin, China  
Rakesh K. Joshi, USA  
Do Kyung Kim, South Korea  
Burtrand I. Lee, USA  
Jun Li, Singapore  
S. J. Liao, China  
Gong-Ru Lin, Taiwan  
J. -Y. Liu, USA  
Jun Liu, USA  
Songwei Lu, USA  
Sanjay Mathur, Germany  
Nobuhiro Matsushita, Japan  
Sherine Obare, USA

P. Panine, France  
Donglu Shi, USA  
Bohua Sun, South Africa  
Maryam Tabrizian, Canada  
Theodore T. Tsotsis, USA  
Y. Wang, USA  
Xiaogong Wang, China  
Michael S. Wong, USA  
Ching Ping Wong, USA  
Ping Xiao, UK  
Zhi-Li Xiao, USA  
Doron Yadlovker, Israel  
Kui Yu, Canada

# Contents

**Emerging Multifunctional Nanostructures**, Hongyou Fan, Yunfeng Lu, Ganapathiraman Ramanath, and José A. Pomposo

Volume 2009, Article ID 281721, 2 pages

**Asymmetric Composite Nanoparticles with Anisotropic Surface Functionalities**, Yilong Wang, Hong Xu, Weili Qiang, Hongchen Gu, and Donglu Shi

Volume 2009, Article ID 620269, 5 pages

**Synthesis and Characterization of Magnetic Nanosized Fe<sub>3</sub>O<sub>4</sub>/MnO<sub>2</sub> Composite Particles**, Zhang Shu and Shulin Wang

Volume 2009, Article ID 340217, 5 pages

**Particle Size and Pore Structure Characterization of Silver Nanoparticles Prepared by Confined Arc Plasma**, Mingru Zhou, Zhiqiang Wei, Hongxia Qiao, Lin Zhu, Hua Yang, and Tiandong Xia

Volume 2009, Article ID 968058, 5 pages

**Vapor Sensing Using Conjugated Molecule-Linked Au Nanoparticles in a Silica Matrix**, Shawn M. Dirk, Stephen W. Howell, B. Katherine Price, Hongyou Fan, Cody Washburn, David R. Wheeler, James M. Tour, Joshua Whiting, and R. Joseph Simonson

Volume 2009, Article ID 481270, 9 pages

**Polyamide 66/Brazilian Clay Nanocomposites**, E. M. Araújo, K. D. Araujo, R. A. Paz, T. R. Gouveia, R. Barbosa, and E. N. Ito

Volume 2009, Article ID 136856, 5 pages

## Editorial

# Emerging Multifunctional Nanostructures

**Hongyou Fan,<sup>1</sup> Yunfeng Lu,<sup>2</sup> Ganapathiraman Ramanath,<sup>3</sup> and José A. Pomposo<sup>4</sup>**

<sup>1</sup>Advanced Materials Laboratory, Sandia National Laboratories, Albuquerque, NM 87106, USA

<sup>2</sup>Chemical and Biomolecular Engineering Department, University of California - Los Angeles (UCLA), CA 90095, USA

<sup>3</sup>Materials Science & Engineering Department, Rensselaer Polytechnic Institute, NY 12180, USA

<sup>4</sup>New Materials Department, Centre for Electrochemical Technologies (CIDETEC), E20009 Donostia-San Sebastián, Spain

Correspondence should be addressed to José A. Pomposo, [jpomposo@cidetec.es](mailto:jpomposo@cidetec.es)

Received 12 February 2009; Accepted 12 February 2009

Copyright © 2009 Hongyou Fan et al. This is an open access article distributed under the Creative Commons Attribution License, which permits unrestricted use, distribution, and reproduction in any medium, provided the original work is properly cited.

The interest in emerging nanostructures is growing exponentially since they are promising building blocks for advanced multifunctional nanocomposites. In recent years, an evolution from the controlled synthesis of individual monodisperse nanoparticles to the tailored preparation of hybrid spherical and also unsymmetrical multiparticle nanostructures is clearly observed. As a matter of fact, the field of nanostructures built around a nanospecies such as inside, outside, and next to a nanoparticle is becoming a new evolving area of research and development with potential applications in improved drug delivery systems, innovative magnetic devices, biosensors, and highly efficient catalysts, among several others.

Emerging nanostructures with improved magnetic, conducting and “smart” characteristics are currently based on the design, synthesis, characterization and modeling of multifunctional nanoobject-based materials. In fact, core-shell nanoparticles and other related complex nanoarchitectures covering a broad spectrum of materials (from metal and metal oxide to fused carbon, synthetic polymer, and biopolymer structures) to nanostructure morphologies (spherical, cylindrical, star-like, etc.) are becoming the main building blocks for next generation of drug delivery systems, advanced sensors and biosensors, or improved nanocomposites. The five papers presented in this special issue examine the preparation and characterization of emerging multifunctional materials, covering from hybrid asymmetric structures to engineering nanocomposites.

In the first paper, the synthesis of nanometer-scale snowman-like asymmetric silica/polystyrene heterostructure with anisotropic functionality offering two-sided biological accessibility is reported. The morphology of the resulting asymmetric composite nanoparticles is illustrated by

TEM images. The interfacial behavior and amphiphilic characteristics of the hybrid nanoparticles as well as their functionalization with two different fluorescent molecules are demonstrated. This multifunctional materials will find important applications in biosensors, cell sorting, and fabrication of smart displays.

In the second paper, magnetic nanosized core-shell  $\text{Fe}_3\text{O}_4/\text{MnO}_2$  composite particles are synthesized by homogeneous precipitation with an  $\text{MnO}_2$  coating thickness of ca. 3 nm as demonstrated by TEM measurements. The hybrid nanoparticles exhibit super paramagnetic properties, and have better dispersivity than the starting materials and better ability of chemical adsorption. The potential use in dyestuff treatment is illustrated by methyl orange decoloration assays.

In the third paper, the confined arc plasma method is employed for the production of silver nanopowders with ultrafine and uniform particle size, high purity, well-dispersed and quasispherical shape. The particle size, lattice parameter, microstructure, morphology, specific surface area, and pore parameters of the silver nanoparticles have been determined by a combination of techniques. This paper open the way to the synthesis of other emerging nanopowders by a convenient, inexpensive, and suitable method for mass production such as the confined arc plasma technique.

In the fourth paper, a simple method to fabricate a chemiresistor-type sensor based on dodecylamine-capped Au nanoparticles (average size 4–6 nm) cross-linked with a phenylene ethynylene oligomer in a silica matrix is reported. This sensor minimizes the swelling transduction mechanism while optimizing the change in dielectric response. In fact, sensors prepared with this methodology show enhanced chemoselectivity for phosphonates which are useful surrogates for chemical weapons.

In the final paper, engineering nanocomposites of polyamide 66 and Brazilian clay are investigated prepared via direct melt intercalation. XRD and TEM techniques are employed to investigate the interlayer spacing and the exfoliation degree in the nanocomposites, respectively. These nanostructured materials exhibit both interesting heat deflection temperatures and good thermal stability, both properties being interesting for industrial applications.

*Hongyou Fan*  
*Yunfeng Lu*  
*Ganapathiraman Ramanath*  
*José A. Pomposo*

## Research Article

# Asymmetric Composite Nanoparticles with Anisotropic Surface Functionalities

Yilong Wang,<sup>1</sup> Hong Xu,<sup>1</sup> Weili Qiang,<sup>1</sup> Hongchen Gu,<sup>1</sup> and Donglu Shi<sup>2,3</sup>

<sup>1</sup>Nano Biomedicine Research Center, Med-X Research Institute, Shanghai Jiao Tong University, Shanghai 200030, China

<sup>2</sup>Department of Chemical and Materials Engineering, University of Cincinnati, Cincinnati, OH 45221, USA

<sup>3</sup>National Key Laboratory of Nano/Micro Fabrication Technology, Research Institute for Micro/Nano Science and Technology, Shanghai Jiao Tong University, Shanghai 200030, China

Correspondence should be addressed to Hongchen Gu, hcgu@sjtu.edu.cn

Received 28 June 2008; Accepted 17 November 2008

Recommended by Jose A. Pomposo

Asymmetric inorganic/organic composite nanoparticles with anisotropic surface functionalities represent a new approach for creating smart materials, requiring the selective introduction of chemical groups to dual components of composite, respectively. Here, we report the synthesis of snowman-like asymmetric silica/polystyrene heterostructure with anisotropic functionalities via a chemical method, creating nanostructure possibly offering two-sided biologic accessibility through the chemical groups. Carboxyl group was introduced to polystyrene component of the snowman-like composites by miniemulsion polymerization of monomer on local surface of silica particles. Moreover, amino group was then grafted to remained silica surface through facile surface modification of the composite nanoparticles. The asymmetric shape of these composites was confirmed by TEM characterization. Moreover, characteristics of anisotropic surface functionalities were indicated by Zeta potential measurement and confocal laser microscopy after being labeled with fluorescent dyes. This structure could find potential use as carriers for biological applications.

Copyright © 2009 Yilong Wang et al. This is an open access article distributed under the Creative Commons Attribution License, which permits unrestricted use, distribution, and reproduction in any medium, provided the original work is properly cited.

## 1. Introduction

Recently, there have been extensive research efforts on the surface functionalization with controlled properties of the colloid particles [1, 2] and the fabrication of the new programmable building blocks for assembly [3]. Several new methods have also been reported on the design and control of the surface functionalization, including deposition of molecules on particles [4], surface-initiated heterophase polymerization [5], and adsorption of colloids [6]. One of the research interests has been focused on the preparation of asymmetrically functionalized particles stemmed from its potential applications in biomedicine due to the fact that the anisotropic particles provide additional functionality compared to their isotropic counterparts [7]. The previously developed methods have been mainly utilized for synthesizing the micrometer scale particles including microcontact printing [8], partial deposition [9, 10], anisotropic decoration [11], gel trapping method [12], laser photochemical deposition [13], micropatterning using a laminar

flow microfluidic device [14], layer-by-layer assembly of polymer [15], and electrohydrodynamic jetting [16, 17]. These asymmetric composites have significantly potential applications in biomedicine and electronic displays due to their asymmetric chemical, physical, and surface properties [18]. However, there have been a few research focused on the development of anisotropically surface-functionalized nanostructures. Therefore, novel methods are critically needed to synthesize composites that are surface functionalized to exhibit high degree of anisotropy in nanoscale.

Here, we report experimental results on the synthesis of nanometer scale, asymmetrically dual-functionalized silica/polystyrene (PS) composites through a chemical approach. That is, a PS nodule with surface carboxyl group and an amino-ended silica particle formed a composite dimer. As will be shown, surface functionalization can take place selectively on either the inorganic or organic surface regions of the composite nanoparticles. Indeed, the synthesized composite nanoparticles possess pronounced structural anisotropy with tunable surface properties.

## 2. Experimental Details

**2.1. Materials.** Tetraethoxysilane (TEOS), ammonium hydroxide (25% w/w), absolute ethanol, triethylamine, toluene, sodium dodecyl sulfate (SDS), sodium bicarbonate, and styrene were purchased from Shanghai Chemical Reagents Company, (Shanghai, China). Hexadecane (99%) and *n*-octadecyltrimethoxysilane (ODMS) were purchased from Acros Organics (NJ, USA). (USA). 3-aminopropyl-triethoxysilane (APS), 4,4'-Azobis(4-cyanopentanoic acid) (ACPA), and tetramethylrhodamine-5-isothiocyanate (TRITC) were purchased from Sigma-Aldrich (MO, USA). 5-(and-6)-carboxyfluorescein succinimidyl ester (NHS-FITC) was purchased from Molecular Probes Inc. (OR, USA). EDC·HCL was purchased from Shanghai Medpep Co. Ltd. (Shanghai, China). Styrene was washed with 5 wt% sodium hydroxide solution first and then with distilled water three times, and stored at 4°C. Deionized water was used for preparation of all aqueous solutions.

**2.2. Synthesis and Local Surface Modification of Silica Particles.** 120 nm monodispersed silica particles were prepared according to the developed Stöber method [19]. Ammonium hydroxide (0.5 M), deionized water (2.1 M), and TEOS (0.12 M) were introduced into 300 cm<sup>3</sup> of absolute ethanol at ambient temperature under vigorous magnetic stirring for 6 hours. 90 cm<sup>3</sup> of TEOS was then added dropwise to the above prepared solution. After 24-hour reaction, the silica particles were collected by centrifugation (9500 rpm for 10 minutes) and frozen dry for 16 hours.

Preparation of the locally modified silica particles: [20, 21] 0.4 cm<sup>3</sup> of ODMS in 20 cm<sup>3</sup> of toluene was impregnated into 0.6 g of the w-silica powder immersed in 0.3 g of water. After addition of 0.8 cm<sup>3</sup> of triethylamine, the suspension was further stirred for 40 hours at room temperature. Then the solid was collected by centrifugation (3000 rpm for 10 minutes) and followed by washing/centrifugation circles with ethanol for three times and thermo treatment at 110°C for 3 hours under vacuum. The obtained locally modified silica particles were kept in a vial until use.

**2.3. Preparation of Asymmetric Composites with Dual Functionalities.** First, the dispersion of 0.1 g locally modified silica particles in the mixture of 4.38 g styrene and 0.17 g hexadecane was introduced into the mixture of 0.114 g SDS, 0.004 g of sodium bicarbonate, and 50 g of deionized water. The whole system was emulsified by stirring at 150 rpm for 1 hour with purged nitrogen. The emulsion was miniemulsified by being ultrasonified at 350 w for 30 minutes. Then under nitrogen protection, the carboxyl-composite particles were obtained by polymerization of styrene initiated by 0.4 g ACPA at 70°C and finished within 3 hours.

Then 0.01 cm<sup>3</sup> APS was added into the dispersion of 35.8 mg carboxyl composite particles in the mixture of 9.1 cm<sup>3</sup> water and 19.9 cm<sup>3</sup> ethanol. The reaction system was magnetically stirred at PH 2.0 for 21 hours and then at PH 12 for 2 hours. At last, the dual-functionalized composites

were obtained when the PH was adjusted back to neutral by several circles of centrifugation and redispersion with water.

**2.4. Labeling the Fluorescence to the Asymmetric Composites.** Labeling the TRITC to the silica part of composites: 0.5 mg TRITC was firstly dissolved in the 11 g absolute ethyl alcohol. 31.4 mg functionalized silica/PS polystyrene composite nanoparticles were dispersed in the 4.8 g absolute ethyl alcohol. The reaction started when the alcohol dispersion of the composites was added in the TRITC alcohol solution rapidly and was magnetically stirred in dark place for 24 hours.

Labeling the NHS-FITC to the PS nodules of the composites: the 2.1 mg EDC·HCL and the 0.7 mg NHS-FITC were dissolved in the 3.5 cm<sup>3</sup> of absolute ethyl alcohol. The 10 mg TRITC labeled composites were dispersed in 1.5 cm<sup>3</sup> of absolute ethyl alcohol. The reaction runs for 5 hours with end-over-end process in dark place after the two dispersions were mixed.

The fluorescence-labeled composite nanoparticles were washed with each 8 cm<sup>3</sup> of ethanol for eleven times to erase the excess TRITC or NHS-FITC by centrifugation/redispersion circles (Sigma Laboratory Centrifuge 3 K 15, Harz, Germany).

**2.5. Characterization.** Transmission electron microscopy (TEM) experiments were performed with a JEOL 2010 microscope (accelerating voltage of 200 kV). Zeta potential measurement was performed at Zetasizer 2000 instruments (Malvern Co., Worcestershire, UK). Confocal micrographs were obtained at Leica TCS SP2 instrument, (Leica Microsystems Co. Ltd., Wetzlar, Germany).

## 3. Results and Discussion

In this case, the negatively charged carboxyl group was loaded on PS part of the composite through miniemulsion polymerization of monomer initiated by an initiator with carboxyl group. The positive amino group was then attached on the silica surface of the composite via grafting with an alkylsilane. Figure 1 illustrates the complete preparation process of the dual functionalized asymmetric composite nanoparticles. As shown in this figure, first, the 120 nm silica particles are prepared. Then, in step (1), the locally modified silica particles are obtained via modification of the partial surface of silica particles by ODMS. In other words, only a limited local region on each silica particle is modified [20, 21]. In step (2), the miniemulsion polymerization of the styrene monomer is performed based on the locally modified silica particles initiated by ACPA. In completion of above steps, the asymmetric silica/PS composite nanoparticles with carboxyl groups on polystyrene surface are prepared. In step (3), grafting of the coupling agent APS on the remained silica surface is performed to introduce the amino groups into the composite nanoparticles. Thus, the dual-functionalized asymmetric composite nanoparticles are obtained. As can be seen in Figure 1, the anisotropic

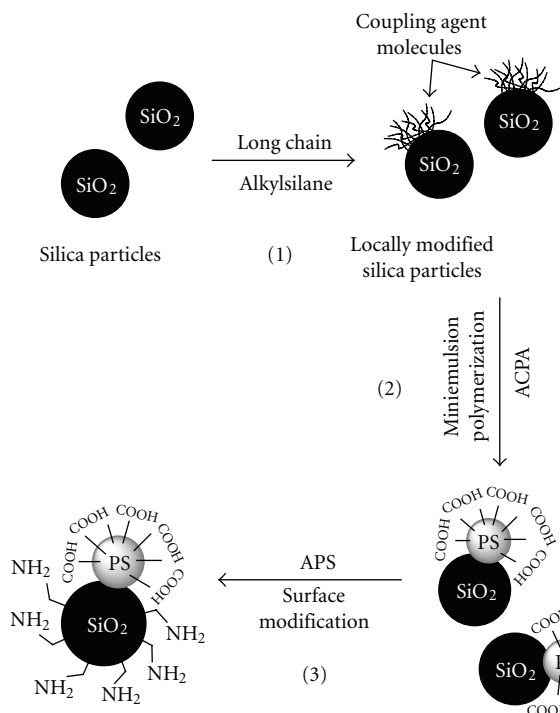
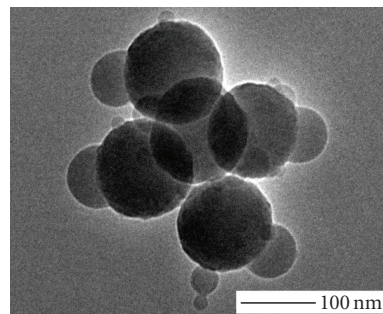


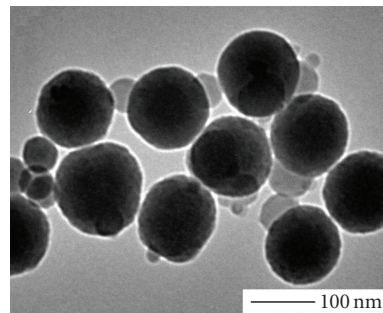
FIGURE 1: Scheme of the pathway for preparation of dual functionalized asymmetric composites nanoparticles.

surface functionalization starts from the miniemulsion polymerization of styrene monomer (step (2)). The asymmetric morphology of the silica/PS composite and the surface carboxyl groups on polystyrene nodules is synchronously created via the miniemulsion polymerization of monomer and local surface modification of silica particles is the key for the formation of the asymmetric inorganic/organic nanocomposites [22]. Due to the selective nucleation and growth of styrene on the partial surface of silica (steps (1) and (2)), further functionalization of the amino group on the remained silica surface can be realized successfully. Thus, as depicted at step (3) in Figure 1, the amino groups are loaded on the silica particles of the composites through grafting of APS.

In this experiment, the anisotropic functionality was established based on the formation of the asymmetric silica/PS composites with snowman-like structure [23]. Figure 2(a) shows the TEM image of the asymmetric composite nanoparticles with carboxyl groups on the surface of PS nodules. The snowman-like pair is composed of a 65 nm polystyrene nodule and a 120 nm silica particle. Figure 2(b) shows the asymmetric nanocomposites with anisotropic dual-functionalities, carboxyl groups on PS nodules, and amino groups on surface of silica particles, respectively. We can see that the composite nanoparticles possessed stable asymmetric morphology after being dually functionalized. Moreover, the asymmetric composites exhibit obvious amphiphilic characteristics. Figure 3 shows comparison of interfacial behavior of the asymmetric composites to that

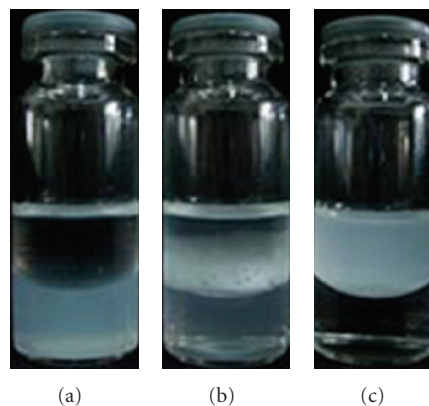


(a)



(b)

FIGURE 2: TEM images of (a) asymmetric nanocomposites with only carboxyl group on the polystyrene nodule, (b) dual-functionalized asymmetric nanocomposites with carboxyl groups on polystyrene nodules and amino groups on silica surface.



(a)

(b)

(c)

FIGURE 3: Photograph of the interfacial behavior of three kinds of particles in the water-toluene dual-phase system: (a) w-SIO particles, (b) asymmetric composite particles, and (c) o-SIO particles.

of pure hydrophilic silica particles (w-SIO) or hydrophobic silica particles (o-SIO) in the water-toluene dual-phase system. It can be seen in Figure 3(b) that asymmetric composite nanoparticles could preferentially exist at the dual-phase interface [24]. In contrast, the unmodified w-SIO particles are dispersed in water (Figure 3(a)), while the o-SIO particles, modified by ODMS thoroughly, are dispersed in toluene (Figure 3(c)).

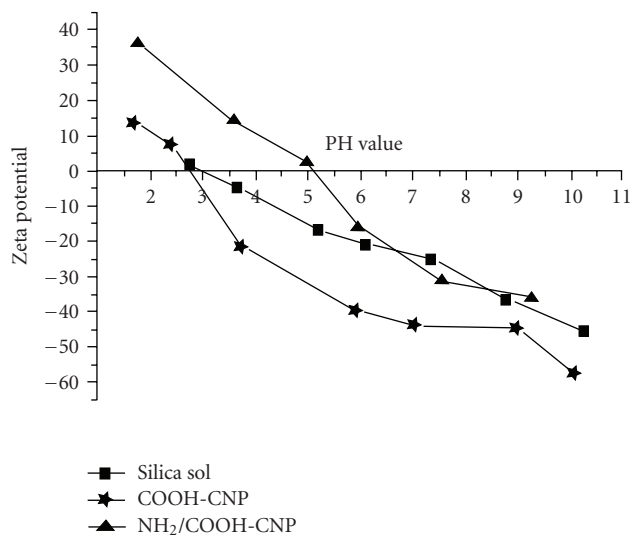
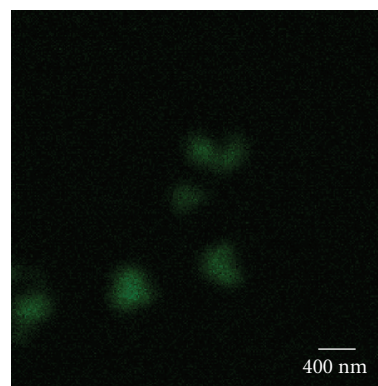


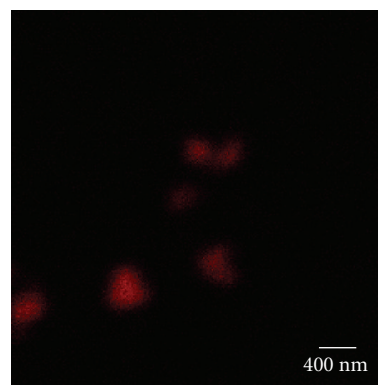
FIGURE 4: Zeta potential curves as a function of PH value of different kinds of particles.

Variation in surface potential of the dual-functionalized composites was characterized by Zeta potential measurement. Figure 4 shows the variation of Zeta potential as a function of PH value. As can be seen, there is obvious difference of the isopotential points between three kinds of aqueous dispersion of the silica particles, carboxyl-ended composite nanoparticles (COOH-CNP), and dual-functionalized composite nanoparticles (NH<sub>2</sub>/COOH-CNP). The isopotential points are 3.2, 2.8, and 5.2, respectively. Meanwhile, the quantity of surface charge of different composites at a certain PH value varies significantly due to different surface functionalities. As can be seen in this figure, the maximum negative charge value of COOH-CNP is about  $-58$  mv at PH 10, slightly higher than  $-45$  mv of silica particles due to the presence of carboxyl groups. In contrast, the positive charge value of the NH<sub>2</sub>/COOH-CNP is about 37 mv, much higher than that of the COOH-CNP at the PH 1.7 due to the presence of the amino groups.

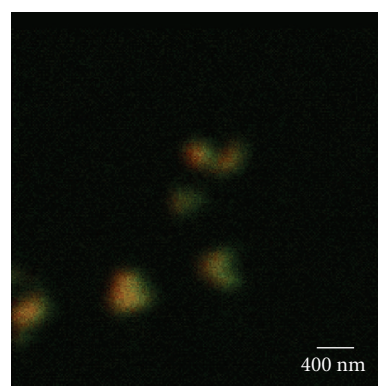
To investigate the possibilities of the as-synthesized dual-functionalized asymmetric composite nanoparticles as the biologic dual-component supporters, the anisotropic functionalities of the composites were labeled with two different fluorescent molecules, respectively. In this case, the dye of TRITC was first used to label the amino group on silica surface through an isothiocyanate functional group that only could be coupled to the amino group of APS specifically. The dye of NHS-FITC was then labeled to the carboxyl group on PS nodules intermediated by EDC·HCL. It is worth noting that TRITC was superfluously used to occupy nearly all available amino groups on the silica surface to avoid the reactions between FITC and remained amino groups. The fluorescent properties of the labeled asymmetric composite were examined by using the confocal laser scanning microscopy (CLSM). Figure 5 shows confocal micrograph of the dual-functionalized composite nanoparticles labeled with two kinds of fluorescences. Figures 5(a) and 5(b)



(a)



(b)



(c)

FIGURE 5: Confocal laser microscopy images showing the dual-functionalized composite particles labeled with different fluorescent molecules: (a) FITC fluorescence; (b) TRITC fluorescence, and (c) overlay. Scale bar: 400 nm.

show the CLSM images obtained at different individual excitation wavelengths of 488 and 543 nm, corresponding to the fluorescences of NHS-FITC and TRITC, respectively. Figure 5(c), superposition of Figures 5(a) and 5(b), indicates the anisotropic fluorescent property of the composite particles with interfacial yellow color, coexisting with the red and green visible from both sides.

The confocal results gave a direct evidence for the anisotropic surface functionalities of the silica/PS composites and the reactive activity of the anisotropic functional groups.

The dual functionalized composite nanoparticles could be used as the selective carriers for two independent ingredients or biological molecules such as DNA or enzyme [25].

#### 4. Conclusion

In conclusion, we have demonstrated a viable synthesis route for making the asymmetric composite nanoparticles with dual functionalities through a two-step chemical approach. The method combining the miniemulsion polymerization of the organic component to local surface modification of the inorganic component may be extended to the introduction of other chemical groups into the asymmetric composite nanoparticles. The as-synthesized composite nanoparticles with controlled distribution of the bioreactive surface functionalities will find important applications in biosensors, cell sorting, and fabrication of smart display.

#### Acknowledgments

This work was supported by National 863 High-Tech Program of China (no. 2006AA032359) and Shanghai Nano Projects (0652nm012, 075207012). The authors thank the Instrumental Analysis Center of Shanghai Jiao Tong University for the materials characterization.

#### References

- [1] R. Davies, G. A. Schurr, P. Meenan, et al., "Engineered particle surfaces," *Advanced Materials*, vol. 10, no. 15, pp. 1264–1270, 1998.
- [2] F. Caruso, "Nanoengineering of particle surfaces," *Advanced Materials*, vol. 13, no. 1, pp. 11–22, 2001.
- [3] S. C. Glotzer, "Materials science: some assembly required," *Science*, vol. 306, no. 5695, pp. 419–420, 2004.
- [4] K. L. Choy, "Chemical vapour deposition of coatings," *Progress in Materials Science*, vol. 48, no. 2, pp. 57–170, 2003.
- [5] W. Zheng, F. Gao, and H. Gu, "Carboxylated magnetic polymer nanolatexes: preparation, characterization and biomedical applications," *Journal of Magnetism and Magnetic Materials*, vol. 293, no. 1, pp. 199–205, 2005.
- [6] S. J. Oldenburg, R. D. Averitt, S. L. Westcott, and N. J. Halas, "Nanoengineering of optical resonances," *Chemical Physics Letters*, vol. 288, no. 2–4, pp. 243–247, 1998.
- [7] M. Yoshida, K.-H. Roh, and J. Lahann, "Short-term biocompatibility of biphasic nanocolloids with potential use as anisotropic imaging probes," *Biomaterials*, vol. 28, no. 15, pp. 2446–2456, 2007.
- [8] O. Cayre, V. N. Paunov, and O. D. Velev, "Fabrication of dipolar colloid particles by microcontact printing," *Chemical Communications*, vol. 9, no. 18, pp. 2296–2297, 2003.
- [9] K. Nakahama, H. Kawaguchi, and K. Fujimoto, "A novel preparation of nonsymmetrical microspheres using the Langmuir-Blodgett technique," *Langmuir*, vol. 16, no. 21, pp. 7882–7886, 2000.
- [10] H. Takei and N. Shimizu, "Gradient sensitive microscopic probes prepared by gold evaporation and chemisorption on latex spheres," *Langmuir*, vol. 13, no. 7, pp. 1865–1868, 1997.
- [11] Y. Fujiki, N. Tokunaga, S. Shinkai, and K. Sada, "Anisotropic decoration of gold nanoparticles onto specific crystal faces of organic single crystals," *Angewandte Chemie International Edition*, vol. 45, no. 29, pp. 4764–4767, 2006.
- [12] V. N. Paunov and O. J. Cayre, "Supraparticles and "Janus" particles fabricated by replication of particle monolayers at liquid surfaces using a gel trapping technique," *Advanced Materials*, vol. 16, no. 9–10, pp. 788–791, 2004.
- [13] E. Hugonnot, A. Carles, M.-H. Delville, P. Panizza, and J.-P. Delville, "'Smart' surface dissymmetrization of microparticles driven by laser photochemical deposition," *Langmuir*, vol. 19, no. 2, pp. 226–229, 2003.
- [14] D. G. Shchukin, D. S. Kommireddy, Y. Zhao, T. Cui, G. B. Sukhorukov, and Y. M. Lvov, "Polyelectrolyte micropatterning using a laminar-flow microfluidic device," *Advanced Materials*, vol. 16, no. 5, pp. 389–393, 2004.
- [15] Z. Li, D. Lee, M. F. Rubner, and R. E. Cohen, "Layer-by-layer assembled Janus microcapsules," *Macromolecules*, vol. 38, no. 19, pp. 7876–7879, 2005.
- [16] K.-H. Roh, D. C. Martin, and J. Lahann, "Biphasic Janus particles with nanoscale anisotropy," *Nature Materials*, vol. 4, no. 10, pp. 759–763, 2005.
- [17] T. Teranishi, "Anisotropically phase-separated biphasic particles," *Small*, vol. 2, no. 5, pp. 596–598, 2006.
- [18] A. Perro, S. Reculosa, S. Ravaine, E. Bourgeat-Lami, and E. Duguet, "Design and synthesis of Janus micro- and nanoparticles," *Journal of Materials Chemistry*, vol. 15, no. 35–36, pp. 3745–3760, 2005.
- [19] W. Stöber, A. Fink, and E. Bohn, "Controlled growth of monodisperse silica spheres in the micron size range," *Journal of Colloid and Interface Science*, vol. 26, no. 1, pp. 62–69, 1968.
- [20] Y. K. Takahara, S. Ikeda, S. Ishino, et al., "Asymmetrically modified silica particles: a simple particulate surfactant for stabilization of oil droplets in water," *Journal of the American Chemical Society*, vol. 127, no. 17, pp. 6271–6275, 2005.
- [21] S. Ikeda, Y. Kowata, K. Ikeue, M. Matsumura, and B. Ohtani, "Asymmetrically modified titanium(IV) oxide particles having both hydrophobic and hydrophilic parts of their surfaces for liquid-liquid dual-phase photocatalytic reactions," *Applied Catalysis A*, vol. 265, no. 1, pp. 69–74, 2004.
- [22] W. Qiang, Y. Wang, P. He, H. Xu, H. Gu, and D. Shi, "Synthesis of asymmetric inorganic/polymer nanocomposite particles via localized substrate surface modification and miniemulsion polymerization," *Langmuir*, vol. 24, no. 3, pp. 606–608, 2008.
- [23] S. Reculosa, C. Poncet-Legrand, A. Perro, et al., "Hybrid dissymmetrical colloidal particles," *Chemistry of Materials*, vol. 17, no. 13, pp. 3338–3344, 2005.
- [24] B. P. Binks, "Particles as surfactants—similarities and differences," *Current Opinion in Colloid & Interface Science*, vol. 7, no. 1–2, pp. 21–41, 2002.
- [25] Y.-Z. Du, T. Tomohiro, G. Zhang, K. Nakamura, and M. Kodaka, "Biotinylated and enzyme-immobilized carrier prepared by hetero-bifunctional latex beads," *Chemical Communications*, vol. 10, no. 5, pp. 616–617, 2004.

## Research Article

# Synthesis and Characterization of Magnetic Nanosized $\text{Fe}_3\text{O}_4/\text{MnO}_2$ Composite Particles

Zhang Shu and Shulin Wang

Department of Power Engineering, University of Shanghai for Science and Technology, 516 Jungong Road, Shanghai 200093, China

Correspondence should be addressed to Shulin Wang, wangshul@online.sh.cn

Received 29 June 2008; Revised 31 August 2008; Accepted 21 October 2008

Recommended by Jose A. Pomposo

Using the prepared  $\text{Fe}_3\text{O}_4$  particles of 10 nm–25 nm as magnetic core, we synthesized  $\text{Fe}_3\text{O}_4/\text{MnO}_2$  composite particles with  $\text{MnO}_2$  as the shell by homogeneous precipitation. Their structure and morphology were characterized by X-ray diffraction (XRD), X-Ray photoelectron spectroscopy (XPS), transmission electronic microscopy (TEM), Fourier transform infrared spectra (FTIR), and vibration-sample magnetometer (VSM). We show that with urea as precipitant transparent and uniform  $\text{MnO}_2$  coating of ca. 3 nm thick on  $\text{Fe}_3\text{O}_4$  particles can be obtained. The composite particles have better dispersivity than the starting materials, and exhibit super-paramagnetic properties and better chemical adsorption ability with saturated magnetization of 33.5 emu/g. Decoloration experiment of methyl orange solution with  $\text{Fe}_3\text{O}_4/\text{MnO}_2$  composite suggested that the highest decoloration rate was 94.33% when the pH of methyl orange solution was 1.3 and the contact time was 50 minutes. So this kind of  $\text{Fe}_3\text{O}_4/\text{MnO}_2$  composite particle not only has super-paramagnetic property, but also good ability of chemical adsorption.

Copyright © 2009 Z. Shu and S. Wang. This is an open access article distributed under the Creative Commons Attribution License, which permits unrestricted use, distribution, and reproduction in any medium, provided the original work is properly cited.

## 1. Introduction

In recent years, nanocomposite materials consisting of core and shell have been attracting great interest and attention of researchers because of their potential application in catalysis, environmental protection, and especially biomedical use. Ikram ul Haq and Egon Matijevic studied the preparation and properties of manganese compounds on hematite in 1997 [1] with three manganese compounds: manganese (II) 2, 4-pentanedionate (MP); manganese (II) methoxide (MMO); and manganese (II) sulfate/urea (MSU) solution under different experimental conditions.

In this paper, we present an approach to synthesize and characterize  $\text{Fe}_3\text{O}_4/\text{MnO}_2$  composite particle by homogeneous precipitation with  $\text{Fe}_3\text{O}_4$  as the magnetic core and  $\text{MnO}_2$  as the shell, where the  $\text{Fe}_3\text{O}_4$  nanoparticles were prepared by coprecipitation method, and the  $\text{Fe}_3\text{O}_4/\text{MnO}_2$  composite core-shell structure was synthesized via hydrolyzation of  $\text{MnSO}_4$  with precipitant. The structures and properties of the materials are discussed in some detail.

## 2. Materials and Methods

**2.1. Preparation of  $\text{Fe}_3\text{O}_4$  Nanoparticles.**  $\text{Fe}_3\text{O}_4$  nanoparticles were prepared by chemical coprecipitation as follows: at first, 2 mol/L NaOH solution and 5% polyethylene glycol (PEG) solution were prepared. 3.24 g of  $\text{FeCl}_3$  and 2.39 g of  $\text{FeCl}_2 \cdot 4\text{H}_2\text{O}$  were dissolved in 100 mL of distilled water, respectively. Then we mixed solutions of  $\text{FeCl}_3$ ,  $\text{FeCl}_2 \cdot 4\text{H}_2\text{O}$ , and 5% PEG together and dispersed them by ultrasonic stirring for 10 minutes. Then the mixture was heated to 75°C, followed by the addition of 2 mol/L NaOH solution until the pH value of the mixture reached about 11.5. The mixing and stirring lasted for 2 hours at 60°C, and then aged at 80°C for 30 minutes. The resulting particles were purified repeatedly by magnetic field separation, washed several times with distilled water or ethanol, and dried at 80°C.

**2.2. Synthesis of  $\text{Fe}_3\text{O}_4/\text{MnO}_2$  Composite by Homogeneous Precipitation.** 0.5 g  $\text{Fe}_3\text{O}_4$  particles were dispersed by ultrasonic stirring in 100 mL 5% PEG for 30 minutes, and were

mixed with 100 mL  $\text{MnSO}_4$  solution of certain concentration, and followed by addition of  $\text{NH}_3 \cdot \text{H}_2\text{O}$  or urea solution. Table 1 shows the experimental conditions. The reaction lasted for 12 hours at  $60^\circ\text{C}$ . At the end of the period, the solids were separated by repeated magnetic separation and washed with distilled water for three times. The products were dried at  $80^\circ\text{C}$  and calcined at  $280^\circ\text{C}$  for 3 hours.

The as-prepared magnetic  $\text{Fe}_3\text{O}_4$  nanoparticles and  $\text{Fe}_3\text{O}_4/\text{MnO}_2$  composite particles were characterized by D/max- $\gamma$ -B X-ray diffractometer (XRD) with  $\text{CuK}\alpha$  radiation, Thermo ESCALAB 250 X-ray photoelectron spectroscopy (XPS) with  $\text{AlK}\alpha$  radiation, and Nicolet 200SXV Fourier transform infrared (FTIR). The morphology of the particle was studied with JEM-2100F transmission electron microscopy (TEM). Magnetic properties of  $\text{Fe}_3\text{O}_4$  and  $\text{Fe}_3\text{O}_4/\text{MnO}_2$  composite particles were investigated by Model-155 vibrating sample magnetometer (VSM).

**2.3. Decoloration Experiment of Methyl Orange Solution with  $\text{Fe}_3\text{O}_4/\text{MnO}_2$  Composite Particles.** 20 mg/L methyl orange solution was prepared as the simulated dye wastewater. The  $\lambda_{\text{max}}$  of methyl orange solution was 465 nm. PH value of the methyl orange solution was regulated to the set value with  $\text{NaOH}$  and  $\text{NH}_3 \cdot \text{H}_2\text{O}$ . 50 mg  $\text{Fe}_3\text{O}_4/\text{MnO}_2$  particles were dispersed by ultrasonic stirring in 50 mL methyl orange solution per time with different pH values for 30 minutes, and absorbance at wavelength of 465 nm was determined by UV-1700 visible spectrophotometer. By calculating the decoloration rate of methyl orange, the appropriate pH value for decoloration was found.

50 mg  $\text{Fe}_3\text{O}_4/\text{MnO}_2$  particles were dispersed by ultrasonic stirring in 50 mL methyl orange solution per time with the appropriate pH value for a different contact time ( $t$ ), and the absorbance at wavelength of 465 nm was also determined. By calculating the discoloration rate of methyl orange, the appropriate contact time value was found too.

### 3. Results and Discussion

**3.1. Structure and Composition of the Materials.** Figure 1 illustrates the X-ray diffraction patterns of the as-manufactured two samples mentioned above. While the lower pattern represents the synthesized standard  $\text{Fe}_3\text{O}_4$  particles, differential peaks appeared at  $2\theta = 27.5^\circ$  and  $2\theta = 40.3^\circ$  in the upper line, which are just the evidence of the existence of  $\text{MnO}_2$  in the  $\text{Fe}_3\text{O}_4/\text{MnO}_2$  composite. Calculating the grain size according to Scherrer formula, we obtained 18.76 nm for the  $\text{Fe}_3\text{O}_4$  particles.

Figure 2 shows the XPS spectrum of Mn and Fe in  $\text{Fe}_3\text{O}_4/\text{MnO}_2$  composite particles. Binding energy of  $\text{Fe}2p_{3/2}$  is 711.1 eV and binding energy of  $\text{Fe}2p_{1/2}$  is 724.6 eV which correspond to the XPS spectrum of  $\text{Fe}_3\text{O}_4$ , and that for  $\text{Mn}2p_{3/2}$  and  $\text{Mn}2p_{1/2}$  are, respectively, 642.2 eV and 653.8 eV. According to the Handbook of X-ray photoelectron spectroscopy [2], the Mn in the composite particles exists as  $\text{Mn}^{4+}$ . These are consistent with the XRD in Figure 1, respectively.

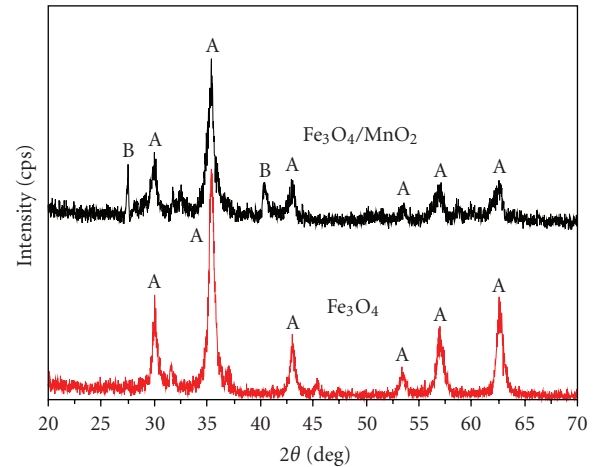


FIGURE 1: XRD patterns of  $\text{Fe}_3\text{O}_4$  and  $\text{Fe}_3\text{O}_4/\text{MnO}_2$  composite particles.

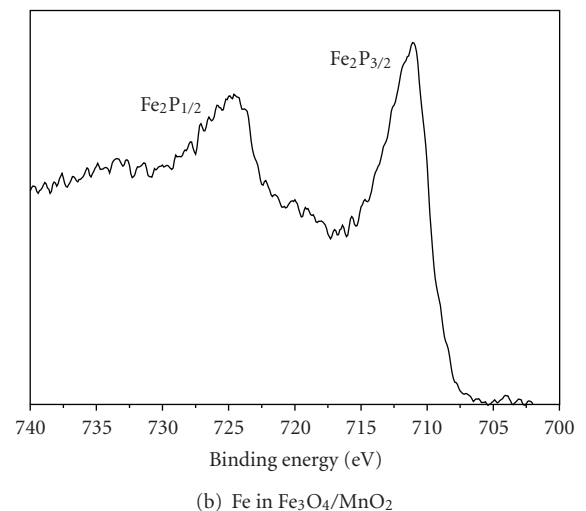
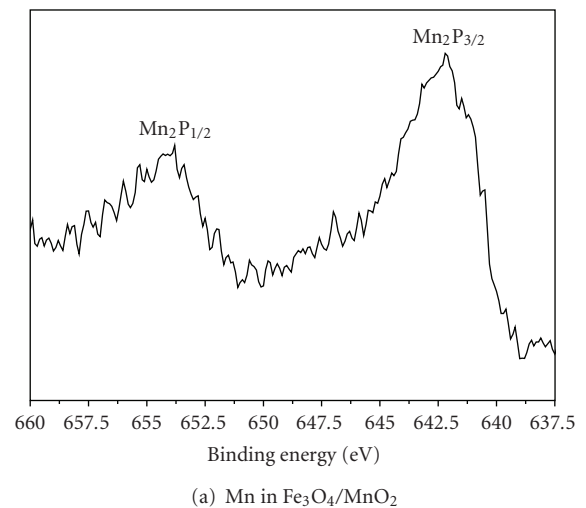


FIGURE 2: XPS spectrum of Mn (a) and Fe (b) in  $\text{Fe}_3\text{O}_4/\text{MnO}_2$  composite particles.

TABLE 1: Reaction condition for synthesis of  $\text{Fe}_3\text{O}_4/\text{MnO}_2$  composite.

Sample	$\text{MnSO}_4/\text{mol}\cdot\text{L}^{-1}$	V(precipitant)/mL	V(PEG)/mL	$\text{Fe}_3\text{O}_4/\text{g}$
(a)	0.072	15(amine)*	100	0.5
(b)	0.072	10(amine)*	100	0.5
(c)	0.036	10(amine)*	100	0.5
(d)	0.036	10(1 mol/L urea)	100	0.5

\* Mass fraction of amine is 25%.

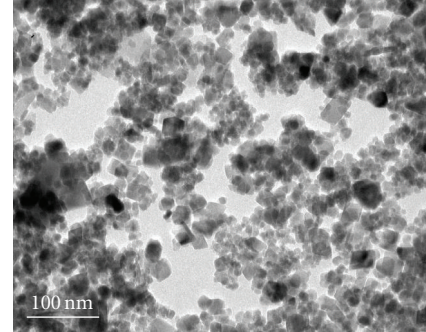
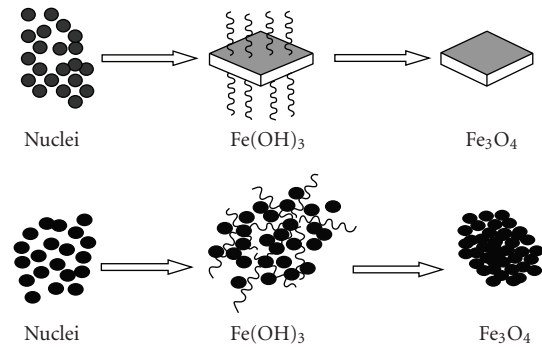
**3.2. Morphology and Shaping Mechanism of  $\text{Fe}_3\text{O}_4$  Nanoparticles.** TEM images of the  $\text{Fe}_3\text{O}_4$  particles are shown in Figure 3. Two different kinds of morphology can be seen some of particles are spherical with diameter of about 10 nm, and the others are square with the diameter of ca.25 nm, it is comparable to that from the XRD pattern in Figure 1.

The reason for the two different particle shapes lies in the different roles the PEG played in the reaction process. At the beginning of the reaction, the amount of PEG was relatively more than that of the  $\text{Fe}(\text{OH})_3$  seed formed in solution because less NaOH was added, part of PEG acted as templates. Certain surface of the  $\text{Fe}(\text{OH})_3$  crystal stopped to grow because of PEG absorbing on it, and in the calcine process the morphology of  $\text{Fe}(\text{OH})_3$  remained, and finally the square shape of the  $\text{Fe}_3\text{O}_4$  particles was formed, this was also observed elsewhere. As more and more NaOH dropped in the solution, the nuclei of  $\text{Fe}(\text{OH})_3$  increased correspondingly, and the effect of dense coating of PEG dominated rather than selective absorption, stopping the  $\text{Fe}(\text{OH})_3$  particles to grow. Finally, small spherical  $\text{Fe}_3\text{O}_4$  nanoparticles were released by the decomposition of  $\text{Fe}(\text{OH})_3$  [3, 4]. Figure 4 shows the schematic shaping mechanism of  $\text{Fe}_3\text{O}_4$  nanoparticles.

**3.3. Morphology and Shaping Mechanism of  $\text{Fe}_3\text{O}_4/\text{MnO}_2$  Composite Particles.** Figures 5(a) and 5(d) present the TEM images of  $\text{Fe}_3\text{O}_4/\text{MnO}_2$  composite particles prepared under different conditions shown in Table 1. Figures 5(a) and 5(b) suggest that by the same concentration of  $\text{MnSO}_4$ , the volumes of  $\text{NH}_3\cdot\text{H}_2\text{O}$  added could affect the thickness of  $\text{MnO}_2$  coating on the  $\text{Fe}_3\text{O}_4$  particles. Though the volume of  $\text{NH}_3\cdot\text{H}_2\text{O}$  was reduced to 10 mL (Table 1), a lot of dissociative  $\text{MnO}_2$  still existed (Figure 5(b)), so we have to reduce further the concentration of  $\text{MnSO}_4$  solution. When the concentration of  $\text{MnSO}_4$  solution was halved, the coating effect was much better as was expected (Figure 5(c)).

To improve the coating, we changed the precipitant from  $\text{NH}_3\cdot\text{H}_2\text{O}$  to urea (1 mol/L). As shown in Figure 5(d), the composite particles look uniformly with darker  $\text{Fe}_3\text{O}_4$  core and transparent  $\text{MnO}_2$  shell, and the coating thickness is ca.3 nm, a demonstration, that the conditions selected are rational.

It is very interesting to show the TEM image of large area in Figure 6, from which we may claim that the  $\text{Fe}_3\text{O}_4/\text{MnO}_2$  core-shell nanoparticles prepared have much better dispersive behavior than the starting materials.

FIGURE 3: TEM image of  $\text{Fe}_3\text{O}_4$  nanoparticles.FIGURE 4: Schematic sketch of the formation of  $\text{Fe}_3\text{O}_4$  with different morphologies.

**3.4. Property for Potential Applications.** Figure 7 shows the hysteresis curves of the  $\text{Fe}_3\text{O}_4$  nanoparticles and the  $\text{Fe}_3\text{O}_4/\text{MnO}_2$  composite particles. The two patterns resemble each other, and also the  $\text{Fe}_3\text{O}_4/\text{MnO}_2$  composite particles have super-paramagnetic properties. With the decreasing of the magnetic field, the magnetization decreased and reached zero at  $H = 0$ , no residual magnetization remained. This prevents particles from aggregation, and the particles can be redispersed rapidly when magnetic field is removed. The saturation magnetization of  $\text{Fe}_3\text{O}_4$  nanoparticles is 68.1 emu/g, and that for the  $\text{Fe}_3\text{O}_4/\text{MnO}_2$  composite particles measured 33.5 emu/g.

The IR spectra of the  $\text{Fe}_3\text{O}_4$  and the  $\text{Fe}_3\text{O}_4/\text{MnO}_2$  composite particles are shown in Figure 8. The characteristic absorption peak of  $\text{Fe}_3\text{O}_4$  lies in  $588.13\text{ cm}^{-1}$ , while that in the  $\text{Fe}_3\text{O}_4/\text{MnO}_2$  composite particles moved to  $606\text{ cm}^{-1}$ , resulting in a blue shift of ca.  $18\text{ cm}^{-1}$ . It may be that the

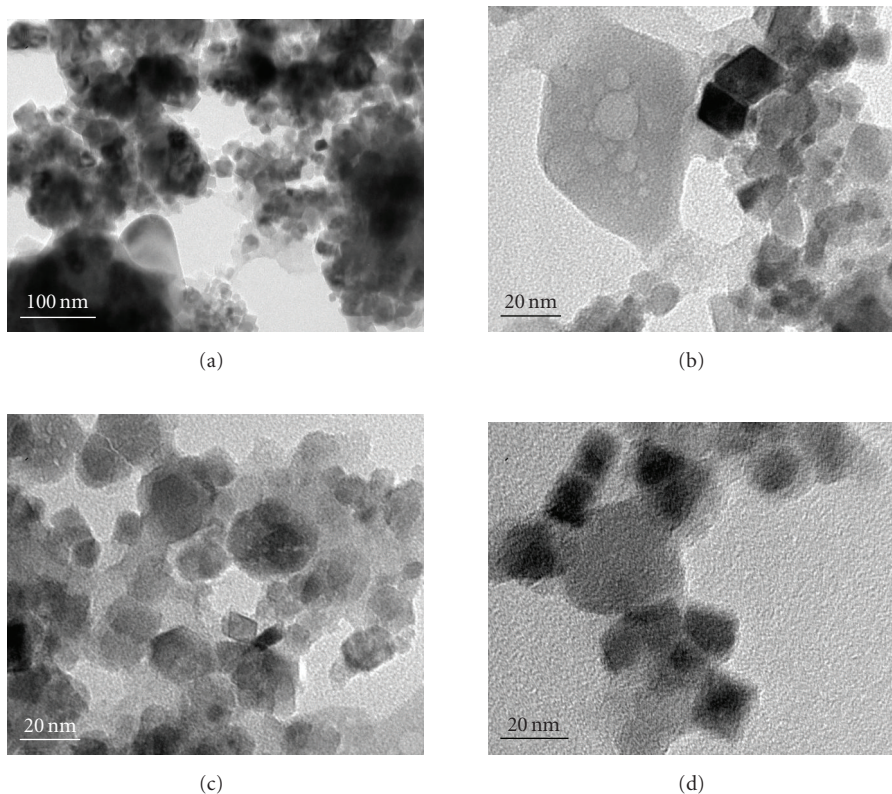


FIGURE 5: TEM images of  $\text{Fe}_3\text{O}_4/\text{MnO}_2$  composite particles prepared under different reaction conditions in Table 1.

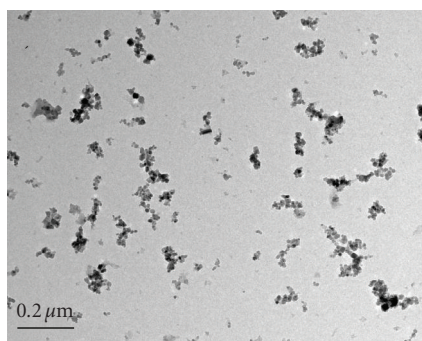
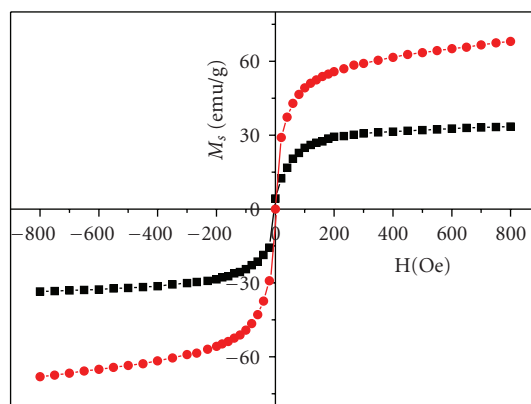


FIGURE 6: TEM images of  $\text{Fe}_3\text{O}_4/\text{MnO}_2$  composite particles in large area.

$\text{Fe}_3\text{O}_4$  particles in the composite were monodispersive in relation to the starting materials. It is significant that there appeared a new peak at  $535\text{ cm}^{-1}$  in the response of the composite particles, implying that there may be some new bond generated between the core and the shell.

The absorption peaks near  $3432\text{ cm}^{-1}$  are flexible vibrating peaks of hydroxy on the surface of composite; it is wider and stronger than that of  $\text{Fe}_3\text{O}_4$ . It means that the composite particles have more hydroxys than  $\text{Fe}_3\text{O}_4$ , which in turn could make  $\text{MnO}_2$  more active. Thus, the composite particles may have better ability of chemical adsorption, which can be used for dyestuff treatment.



—■—  $\text{Fe}_3\text{O}_4/\text{MnO}_2$   
—●—  $\text{Fe}_3\text{O}_4$

FIGURE 7: Magnetic hysteresis loop of  $\text{Fe}_3\text{O}_4$ ,  $\text{Fe}_3\text{O}_4/\text{MnO}_2$  composite particles.

Then the decoloration of methyl orange with  $\text{Fe}_3\text{O}_4/\text{MnO}_2$  was studied, and the influence of initial solution pH value and contact time on the decoloration was investigated. Figures 9(a) and 9(b) suggest that pH value is the key factor influencing decoloration efficiency. The lower pH value and adequate contact time ( $t$ ) are favorable for the methyl orange

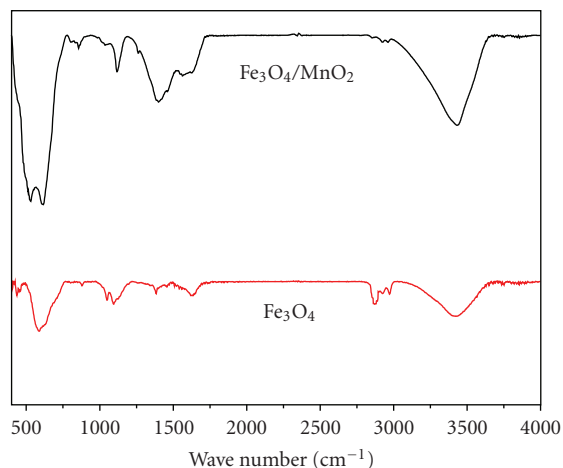


FIGURE 8: IR spectrum of samples  $\text{Fe}_3\text{O}_4$ ,  $\text{Fe}_3\text{O}_4/\text{MnO}_2$  composite particles.

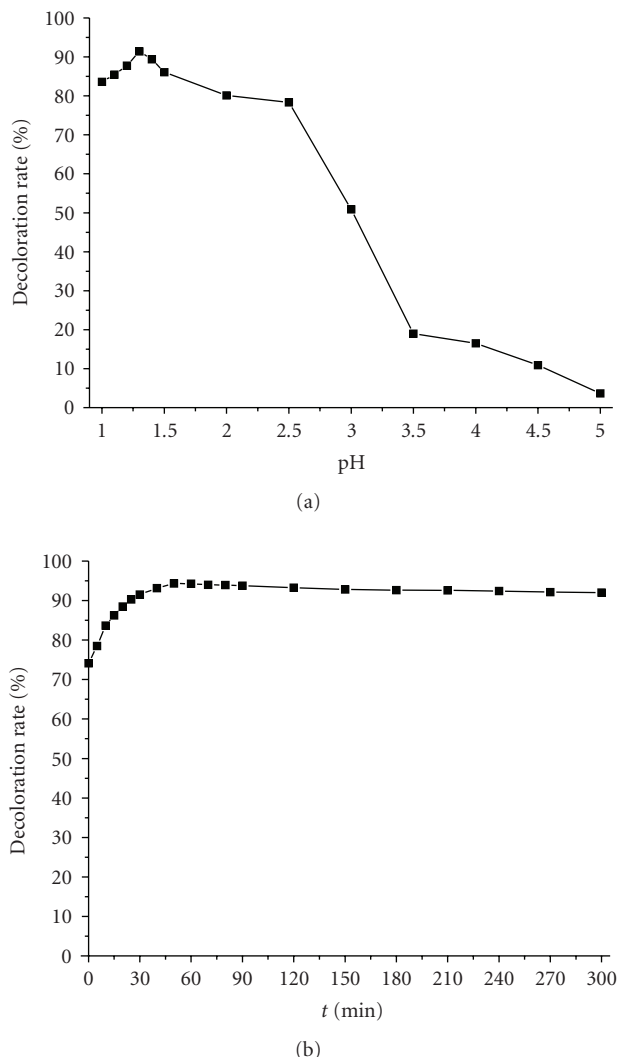


FIGURE 9: Effect of pH value (a) and contact time (b) on decoloration rate.

solution decoloration. With the same contact time ( $t = 30$  minutes), the highest decoloration rate was 91.4% when the  $\text{pH} = 1.3$ , and it can reach the highest decoloration rate 94.33% when the contact time was 50 minutes. So this kind of  $\text{Fe}_3\text{O}_4/\text{MnO}_2$  composite particle not only has super-paramagnetic property, but also has good ability of chemical adsorption which may find wide applications in the field of dyestuff adsorption.

#### 4. Conclusion

Using the prepared  $\text{Fe}_3\text{O}_4$  particles of 10 nm–25 nm as magnetic core, we synthesized  $\text{Fe}_3\text{O}_4/\text{MnO}_2$  composite particles with  $\text{MnO}_2$  as the shell by homogeneous precipitation. The composite particles look uniformly with darker  $\text{Fe}_3\text{O}_4$  core and transparent  $\text{MnO}_2$  shell, and the coating thickness is ca.3 nm. The as-synthesized  $\text{Fe}_3\text{O}_4/\text{MnO}_2$  composite particles exhibit super-paramagnetic properties and have better dispersivity than the starting materials. The saturation magnetization of  $\text{Fe}_3\text{O}_4$  nanoparticles is 68.1 eum/g, and that for the  $\text{Fe}_3\text{O}_4/\text{MnO}_2$  composite particles measured 33.5 eum/g. Decoloration experiment of methyl orange solution with  $\text{Fe}_3\text{O}_4/\text{MnO}_2$  composite suggests that the highest decoloration rate is 94.33% when the pH value of methyl orange solution was 1.3 and the contact time was 50 minutes. So this kind of  $\text{Fe}_3\text{O}_4/\text{MnO}_2$  composite particle not only has super-paramagnetic property but also has good ability of chemical adsorption.

#### References

- [1] I. ul Haq and E. Matijević, "Preparation and properties of uniform coated inorganic colloidal particles," *Journal of Colloid and Interface Science*, vol. 192, no. 1, pp. 104–113, 1997.
- [2] C. D. Wagner, W. M. Riggs, M. E. Davis, S. F. Moulder, and G. E. Muilenberg, *Handbook of X-Ray Photoelectron Spectroscopy*, Perkin-Elmer, New York, NY, USA, 1996.
- [3] Z. Zhang, H. Sun, X. Shao, D. Li, H. Yu, and M. Han, "Three-dimensionally oriented aggregation of a few hundred nanoparticles into monocrystalline architectures," *Advanced Materials*, vol. 17, no. 1, pp. 42–47, 2005.
- [4] J. C. Yu, A. Xu, L. Zhang, R. Song, and L. Wu, "Synthesis and characterization of porous magnesium hydroxide and oxide nanoplates," *The Journal of Physical Chemistry B*, vol. 108, no. 1, pp. 64–70, 2004.

## Research Article

# Particle Size and Pore Structure Characterization of Silver Nanoparticles Prepared by Confined Arc Plasma

Mingru Zhou,<sup>1,2</sup> Zhiqiang Wei,<sup>2,3</sup> Hongxia Qiao,<sup>1,2</sup> Lin Zhu,<sup>3</sup> Hua Yang,<sup>3</sup> and Tiandong Xia<sup>2</sup>

<sup>1</sup> School of Civil Engineering, Lanzhou University of Technology, Lanzhou 730050, China

<sup>2</sup> State Key Laboratory of Advanced New Nonferrous Materials, Lanzhou University of Technology, Lanzhou 730050, China

<sup>3</sup> School of Science, Lanzhou University of Technology, Lanzhou 730050, China

Correspondence should be addressed to Zhiqiang Wei, zqwei7411@163.com

Received 24 September 2008; Accepted 18 November 2008

Recommended by Jose A. Pomposo

In the protecting inert gas, silver nanoparticles were successfully prepared by confined arc plasma method. The particle size, microstructure, and morphology of the particles by this process were characterized via X-ray powder diffraction (XRD), transmission electron microscopy (TEM) and the corresponding selected area electron diffraction (SAED). The N<sub>2</sub> adsorption-desorption isotherms of the samples were measured by using the static volumetric absorption analyzer, the pore structure of the sample was calculated by Barrett-Joyner-Halenda (BJH) academic model, and the specific surface area was calculated from Brunauer-Emmett-Teller (BET) adsorption equation. The experiment results indicate that the crystal structure of the samples is face-centered cubic (FCC) structure the same as the bulk materials, the particle size distribution ranging from 5 to 65 nm, with an average particle size about 26 nm obtained by TEM and confirmed by XRD and BET results. The specific surface area is 23.81 m<sup>2</sup>/g, pore volumes are 0.09 cm<sup>3</sup>/g, and average pore diameter is 18.7 nm.

Copyright © 2009 Mingru Zhou et al. This is an open access article distributed under the Creative Commons Attribution License, which permits unrestricted use, distribution, and reproduction in any medium, provided the original work is properly cited.

## 1. Introduction

Nanoparticles exhibit novel properties that significantly different from those of corresponding bulk solid-state owing to the small size effect, surface effect, quantum size effect and quanta tunnel effect [1–5]. During the past years, the investigation for metal nanoparticles has attracted considerable attention due to their novel physical and chemical properties and potential application in diverse areas, such as catalyst, microelectronic elements, photoelectronic devices, lubricants, conductive materials, activation, and sintering materials [6–11]. All these application aspects require the powders consisting of monodisperse particles with desired physical and chemical properties. Many unique properties of nanocrystalline materials are mainly related to the particle size and pore structure [12–16]. The investigation on the particle size and pore structure for nanoparticles is essential to fully understand the structure of a nanocrystalline material as well as to the explanation of the intriguing properties, and it offers the possibility to obtain nanoparticles with desired physical and chemical properties.

Arc plasma method is a mature and advanced materials processing technique, and many metal nanoparticles have successfully been prepared by this method in the past [16–18]. Compared with the conventional methods, confined arc plasma method has been proven to be suitable for production of metal nanopowders with ultrafine particle size, higher purity, narrow size distribution, well dispersed, and spherical shape. In addition, the physical and chemical properties of the nanopowders by this method can be easily improved by varying the processing parameters. Especially, it is a convenient, inexpensive process, and suitable for mass production in the industry [19]. However, to the best of our knowledge, there is no report on the preparation of uniform and monodisperse Ag nanoparticles in high yield by arc plasma method. In this paper, silver nanoparticles were successfully prepared by confined arc plasma technique in inert atmosphere. In addition, the particle size, lattice parameter, microstructure, morphology, specific surface area, and pore parameters of the samples by this process were characterized via X-ray powder diffraction (XRD), transmission electron microscopy (TEM), the corresponding selected area electron

diffraction (SAED), and static volumetric absorption analyzer, and the results were discussed.

## 2. Experimental

Silver nanoparticles were prepared by confined arc plasma technique in inert atmosphere with home-made experimental apparatus described elsewhere [18, 19]. In the process of preparation, the vacuum chamber was pumped to  $10^{-3}$  Pa and then was backfilled with inert gas near to  $10^3$  Pa. The electric arc in the inert environment was automatically ignited between the wolfram electrode and the nozzle by high-frequency initiator. Under argon pressure and electric discharge current, the ionized gases were driven through the nozzle outlet and form the plasma jet [20]. The bulk metal silver (purity 99.99%) was heated and melted by the high temperature of the plasma, metal atom detached from the metal surface when the plasma jet kinetic energy exceeds the metal superficial energy and evaporated into atom soot. Above the evaporation source, there is a region filled with supersaturated metal vapor, where the metal atoms diffused around and collided with each other to decrease the nuclei forming energy. When the metal vapor was supersaturated, a new phase was nucleated homogeneously out of the aerosol systems [21]. The droplets were rapidly cooled and combined to form primary particles by an aggregation growth mechanism [22]. The free inert gas convection between the hot evaporation source and the cooled collection cylinder transported the particles out of this nucleation and growth region to the inner walls of the cylinder. The loose nanoparticles could be obtained after a period of passivation and stabilization with working gas.

Table 1 shows the referential technological parameters of preparing silver nanoparticles by confined arc plasma method. To investigate the structure of the samples, the as-obtained nanoparticles were analyzed by a rotating target X-ray diffractometer (Japan Rigaku D/Max-2400) equipped with a monochromatic high-intensity Cu K $\alpha$  radiation ( $\lambda = 1.54056 \text{ \AA}$ , 40 kV, 100 mA), The X-ray powder diffraction data were recorded in a range from 30 to  $100^\circ$  ( $2\theta$ ) with scanning rate  $0.005^\circ/\text{s}$  and step size  $0.02^\circ$ . The average grain size of the nanoparticles was estimated from the half-maximum width and the peak position of an XRD line broadened according to the Scherrer formula.

The particle size and morphology of the sample and the corresponding selected area electron diffraction (SAED) were examined by transmission electron microscopy (TEM) and Japan JEOL JEM-1200EX microscope with an accelerating voltage of 80 kv, respectively. In the process of preparation of the TEM specimen, a small amount of the powders was dispersed in a few milliliters of normal butanol in an ultrasonic bath and sonicated for 30 minutes, and a drop from an eye dropper of this dispersion sample was placed on a copper grid coated with holey carbon film. The samples were placed in a vacuum oven to dry at ambient temperature before examining. The sample is scanned in all zones before the picture is taken.

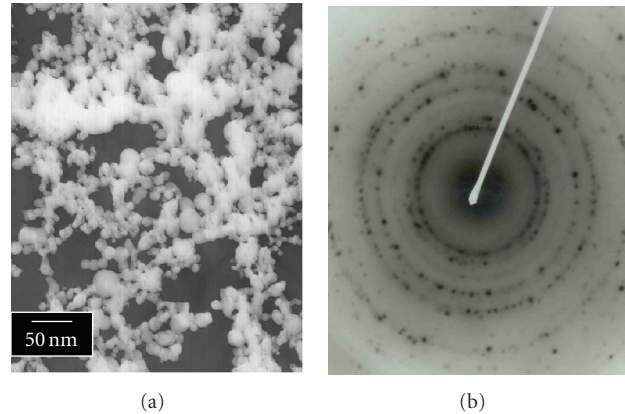


FIGURE 1: (a) TEM micrograph and (b) the selected area electron diffraction pattern of Ag nanoparticles.

The  $N_2$  absorption-desorption isotherms of the samples at liquid nitrogen temperature (78 K) and gas saturation vapor tension range were measured by using the ASAP 2010 static volumetric absorption analyzer produced by Micromeritics Corp., NY, USA. Approximately 0.3 to 0.5 g of powder were placed in a test tube and allowed to degas for 2 hours at  $175^\circ\text{C}$  in flowing nitrogen. This removes contaminants such as water vapor and adsorbed gases from the samples. The static physisorption isotherms were obtained with  $N_2$  in liquid nitrogen, the amount of liquid nitrogen adsorption, or desorption from the material as a function of pressure ( $P/P_0 = 0.025 - 0.999$ ). Data were obtained by admitting or removing a known quantity of adsorbing gas in or out of a sample cell containing the solid adsorbent maintained at a constant temperature (77.35 K). As adsorption or desorption occurs, the pressure in the sample cell changes until equilibrium is established. From the  $N_2$  static physisorption isotherm of the samples to obtain the single layer adsorption capacity, the specific surface area of the sample was calculated from the BET adsorption equation. Based on the BJH academic model, the properties of the cumulative pore specific surface area, cumulative pore volume, average pore diameter, and BJH desorption pore distribution curves of the samples were estimated by BJH analysis method.

## 3. Results and Discussion

Figure 1(a) shows the representative transmission electron microscopy image of Ag nanoparticles. The TEM observation shows that the morphology of Ag nanoparticles is monodisperse; most of them are quasispherical shapes with smooth surface and uniform size. Some small particles aggregate into secondary particles because of their extremely small dimensions and high-surface energy.

Figure 1(b) shows the corresponding selected area electron diffraction (SAED) pattern. It can be indexed to the reflection of face-centered cubic (FCC) structure in crystallography, and this result was also investigated by means of X-ray diffraction. Tropism of the particles at random

TABLE 1: Referential technological parameters of preparing metal nanoparticles by confined arc plasma.

Gas pressure	Atmosphere	Arc voltage	Arc current	Cooled condition	Yield rate	Particle size
0.4 ~ 1.4 KPa	He, N <sub>2</sub> , Ar	20 ~ 30 V	60 ~ 160 A	Water	0.5 ~ 1.3 g/min	20 ~ 100 nm

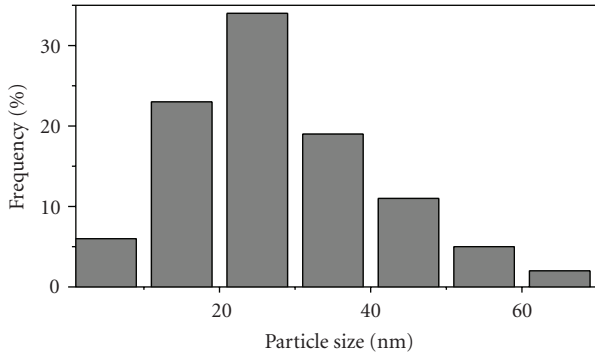


FIGURE 2: Particle size distribution of Ag nanoparticles.

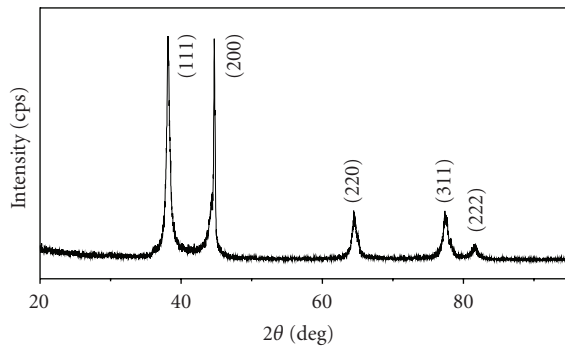
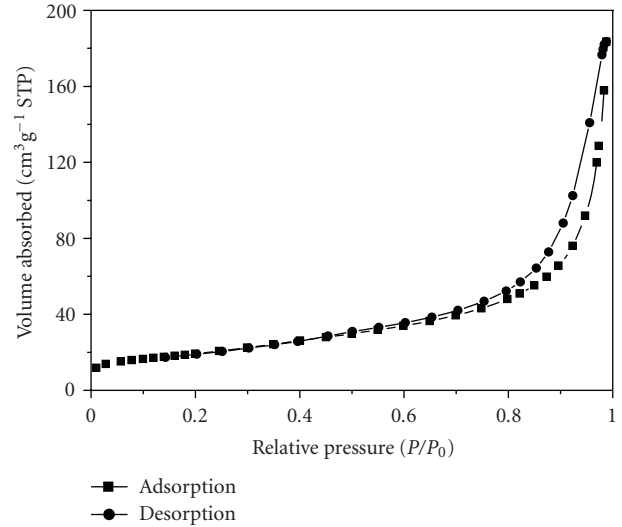


FIGURE 3: XRD patterns of Ag nanoparticles.

and small particles causes the widening of diffraction rings that made up of many diffraction spots, which indicate that the nanoparticles are polycrystalline structure. Electron diffraction reveals that each particle is composed of many small crystal nuclei, which is a convincing proof that the particles grow in an aggregation model.

From the data obtained by TEM micrographs, the particle size histograms can be drawn, and the mean size of the particles can be determined. Figure 2 shows the particle size distribution of Ag nanoparticles. It can be seen that the particle sizes range is from 5 nm to 65 nm, and the median diameter (taken as average particle diameter) is about 26 nm, being deduced from the images, which shows a relatively broad size distribution.

Figure 3 shows the typical X-ray diffraction pattern for the specimen. The diffraction peaks are broad, suggesting that the sample consists of very small particles. The major peaks of the pure Ag powders are observed. Five broad peaks with  $2\theta$  values of  $38.14^\circ$ ,  $44.70^\circ$ ,  $64.57^\circ$ ,  $77.37^\circ$ , and  $81.69^\circ$  corresponding to the (111), (200), (220), (311), and (222) planes of the bulk Ag, respectively, which can be assigned to Ag FCC structure. The XRD pattern shows that the samples

FIGURE 4: N<sub>2</sub> adsorption-desorption isotherms of Ag nanoparticles.

are single phase, and no other distinct diffraction peak, except the characteristic peaks of FCC phase Ag, was found.

From the full width at half maximum, the grain size for the sample can be calculated from half widths of the major diffraction peak (111) according to Scherrer formula,  $d = K\lambda/B \cos\theta$ , where  $d$  is the grain size,  $K = 0.89$  is the Scherrer constant related to the shape and index (hkl) of the crystals,  $\lambda$  is the wavelength of the X-ray (Cu K $\alpha$ , 1.54056 Å),  $\theta$  is the diffraction angle, and  $B$  is the corrected full width at half maximum (in radian). The average crystallite size was found to be about 24 nm, which is well consistent with the average particle diameter obtained from TEM images of Figure 2(a).

According to the electron diffraction formula  $Rd_{hkl} = \lambda L$  and the X-ray diffraction  $\lambda = 2d_{hkl} \cos\theta$ , the values of interplaner spacings  $d_{hkl}$  were calculated from the diameters of the diffraction rings as well as from the results of the XRD analysis. For FCC structure,  $d_{hkl} = a/\sqrt{h^2 + k^2 + l^2}$ , the lattice parameter ( $a$ ) can be calculated from measured values for the spacing of the (111) plane, respectively. Table 2 presents the results of the lattice parameter and the interplaner spacings measured in the TEM-SAED and XRD analyses, and compares them to standard ASTM data ( $a = 4.088$  Å), the lattice constriction was found.

The N<sub>2</sub> adsorption-desorption isotherms of the samples were measured by using the static volumetric absorption analyzer. Figure 4 shows the typical nitrogen sorption isotherms of Ag nanoparticles. It shows the sample presents typical IV adsorption, in the low-pressure region ( $P/P_0 < 0.7$ ). It can be seen from the graph that the isotherms relative flat, namely, the adsorption and desorption isotherms completely superposition, owing to the adsorption of the samples mostly occurs in the micropores. At the relative high pressure

TABLE 2: Comparison of interplaner spacings ( $d_{hkl}$ ) and the lattice parameter ( $a$ ) with standard ASTM data.

Method	TEM (Å)	XRD (Å)	ASTM standard value (Å)
Interplaner spacings ( $d_{hkl}$ )	2.978	2.977	2.980
Lattice parameter ( $a$ )	4.086	4.084	4.088

TABLE 3: BET experimental results of Ag nanoparticles.

Constant C	Monolayer adsorption volume $V_m$	BET surface area $S_{BET}$	Average particle size $D_{BET}$
32.7754	2.4258 cm <sup>3</sup> /g	23.81 m <sup>2</sup> /g	28 nm

TABLE 4: Pore structure parameters of Ag nanoparticles.

Cumulative surface area of pores $S_{BJH}$	Cumulative pore volume of pores $V_{BJH}$	Average pore diameter $d_{BJH}$	Probability pore size $D$
18.91 m <sup>2</sup> /g	0.0882 cm <sup>3</sup> g <sup>-1</sup>	18.7 nm	23 nm

region ( $P/P_0 > 0.7$ ), due to the capillary agglomeration phenomenon, the isotherms increase rapidly and form a lag loop.

Figure 5 shows BET plots of Ag nanoparticles. The specific surface area of Ag nanopowder calculated using the multipoint BET-equation is 23.81 m<sup>2</sup>/g. Assuming that the particles have solid, spherical shape with smooth surface, and same size, the surface area can be related to the average equivalent particle size by the equation  $D_{BET} = 6000/(\rho \cdot S_w)$  (in nm), where  $D_{BET}$  is the average diameter of a spherical particle,  $S_w$  represents the measured surface area of the powder in m<sup>2</sup>/g, and  $\rho$  is the theoretical density in g/cm<sup>3</sup>. Table 3 presents the BET experimental results of Ag nanoparticles. We noticed that the particle size obtained from the BET and the TEM methods agrees very well with the result given by X-ray line broadening. The results of TEM observations and BET methods further confirmed and verified the relevant results obtained by XRD as mentioned above.

Figure 6 shows the typical BJH desorption pore size distribution curves of Ag nanopowder. From the curves, we can see that most of the micropores with a size smaller than 40 nm, the probability pore size of which estimated from the peak position is about 23 nm, and possesses a relatively narrow pore size distribution. Moreover, such micropores have not been observed within particles by TEM (see Figure 2). Therefore, these particles are actually grain clusters, that is, small polycrystals. Based on the BJH academic model, the property of the cumulative pore specific surface area, cumulative pore volume, average pore diameter, and the probability pore size of pores were calculated by BJH analysis method and summarized in Table 4.

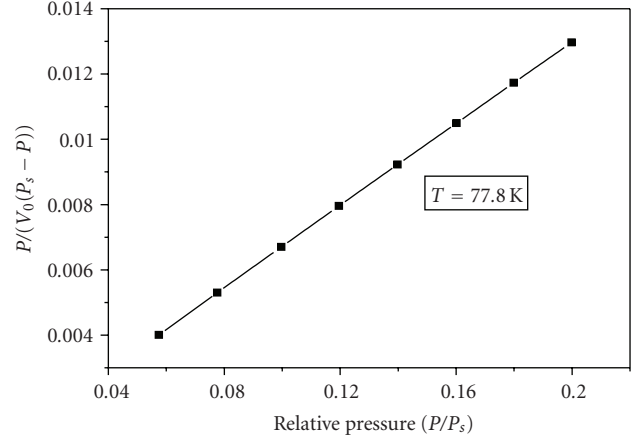


FIGURE 5: BET plots of Ag nanoparticles.

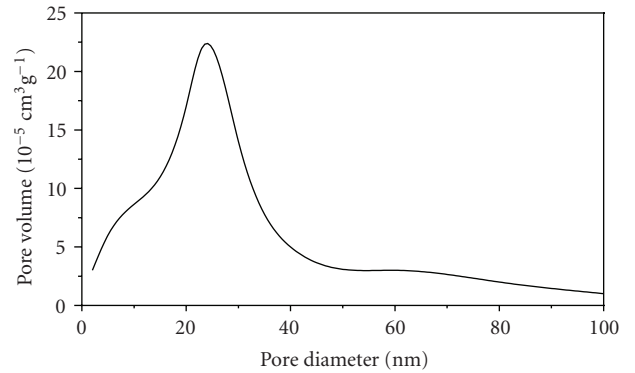


FIGURE 6: BJH pore size distribution curves of Ag nanoparticles.

## 4. Conclusions

(1) Silver nanoparticles were successfully prepared by confined arc plasma method in the protecting inert atmosphere. The nanoparticles prepared by this method achieved uniform particle size, higher purity, well-dispersed and quasispherical shape.

(2) The crystalline structure of the particles is FCC structure the same as that of the bulk materials, the particle size distribution ranges from 5 to 65 nm with average particle size about 26 nm, the average equivalent particle size obtained from the TEM and confirmed by XRD and BET results.

(3) The specific surface area of the sample is 23.81 m<sup>2</sup>/g calculated from the BET adsorption equation. Based on the BJH academic model, the cumulative pore specific surface area, the cumulative pore volume, the average pore diameter, and the probability pore size of the samples are 18.91 m<sup>2</sup>/g, 0.0882 cm<sup>3</sup>/g, 18.7 nm, and 23 nm, respectively.

## Acknowledgments

This work was supported by the Key Project of Chinese Ministry of Education (no. 208151), Natural Science Foundation of Gansu Province, China (no. 2007GS04821), and Scientific

Research Developmental Foundation of Lanzhou University of Technology (no. SB10200805).

## References

- [1] H. Gleiter, "Nanocrystalline materials," *Progress in Materials Science*, vol. 33, no. 4, pp. 223–315, 1990.
- [2] Y. J. Chen, M. S. Cao, Q. Tian, T. H. Wang, and J. Zhu, "A novel preparation and surface decorated approach for  $\alpha$ -Fe nanoparticles by chemical vapor-liquid reaction at low temperature," *Materials Letters*, vol. 58, no. 9, pp. 1481–1484, 2004.
- [3] W.-W. Zhang, Q.-Q. Cao, J.-L. Xie, et al., "Structural, morphological, and magnetic study of nanocrystalline cobalt-nickel-copper particles," *Journal of Colloid and Interface Science*, vol. 257, no. 2, pp. 237–243, 2003.
- [4] Z. L. Cui, L. F. Dong, and C. C. Hao, "Microstructure and magnetic property of nano-Fe particles prepared by hydrogen arc plasma," *Materials Science and Engineering A*, vol. 286, no. 1, pp. 205–207, 2000.
- [5] H. Gleiter, "Materials with ultrafine microstructures: retrospective and perspectives," *Nanostructured Materials*, vol. 1, no. 1, pp. 1–19, 1992.
- [6] B. J. Chen, X. W. Sun, C. X. Xu, and B. K. Tay, "Growth and characterization of zinc oxide nano/micro-fibers by thermal chemical reactions and vapor transport deposition in air," *Physica E*, vol. 21, no. 1, pp. 103–107, 2004.
- [7] D. Chen, D. Chen, X. Jiao, Y. Zhao, and M. He, "Hydrothermal synthesis and characterization of octahedral nickel ferrite particles," *Powder Technology*, vol. 133, no. 1–3, pp. 247–250, 2003.
- [8] M. S. Cao and Q. G. Deng, "Synthesis of nitride-iron nano meter powder by thermal chemical vapor-phase reaction method," *Journal of Inorganic Chemistry*, vol. 12, no. 1, pp. 88–91, 1996.
- [9] J. Karthikeyan, C. C. Berndt, J. Tikkanen, S. Reddy, and H. Herman, "Plasma spray synthesis of nanomaterial powders and deposits," *Materials Science and Engineering A*, vol. 238, no. 2, pp. 275–286, 1997.
- [10] H. Zheng, J. Lang, J. Zeng, and Y. Qian, "Preparation of nickel nanopowders in ethanol-water system (EWS)," *Materials Research Bulletin*, vol. 36, no. 5–6, pp. 947–952, 2001.
- [11] G. F. Gaertner and H. Lydtin, "Review of ultrafine particle generation by laser ablation from solid targets in gas flows," *Nanostructured Materials*, vol. 4, no. 5, pp. 559–568, 1994.
- [12] J. L. Katz and P. F. Miquel, "Syntheses and applications of oxides and mixed oxides produced by a flame process," *Nanostructured Materials*, vol. 4, no. 5, pp. 551–557, 1994.
- [13] B. Günther and A. Kumpmann, "Ultrafine oxide powders prepared by inert gas evaporation," *Nanostructured Materials*, vol. 1, no. 1, pp. 27–30, 1992.
- [14] D. Vollath and K. E. Sickafus, "Synthesis of nanosized ceramic oxide powders by microwave plasma reactions," *Nanostructured Materials*, vol. 1, no. 5, pp. 427–437, 1992.
- [15] D.-H. Chen and X.-R. He, "Synthesis of nickel ferrite nanoparticles by sol-gel method," *Materials Research Bulletin*, vol. 36, no. 7–8, pp. 1369–1377, 2001.
- [16] I. Bica, "Nanoparticle production by plasma," *Materials Science and Engineering B*, vol. 68, no. 1, pp. 5–9, 1999.
- [17] X. Li and S. Takahashi, "Synthesis and magnetic properties of Fe-Co-Ni nanoparticles by hydrogen plasma-metal reaction," *Journal of Magnetism and Magnetic Materials*, vol. 214, no. 3, pp. 195–203, 2000.
- [18] Z. Q. Wei, H. X. Qiao, and P. X. Yan, "Particle size and microstructure of Ni nanoparticles by anodic arc plasma," *Acta Metallurgica Sinica*, vol. 18, no. 3, p. 209, 2005.
- [19] Z. Wei, T. Xia, L. Bai, J. Wang, Z. Wu, and P. Yan, "Efficient preparation for Ni nanopowders by anodic arc plasma," *Materials Letters*, vol. 60, no. 6, pp. 766–770, 2006.
- [20] A. Anders and J. W. Kwan, "Arc-discharge ion sources for heavy ion fusion," *Nuclear Instruments and Methods in Physics Research Section A*, vol. 464, no. 1–3, pp. 569–575, 2001.
- [21] C. Kaito, "Coalescence growth mechanism of smoke particles," *Japanese Journal of Applied Physics*, vol. 24, no. 3, pp. 261–264, 1985.
- [22] J. H. J. Scott and S. A. Majetich, "Morphology, structure, and growth of nanoparticles produced in a carbon arc," *Physical Review B*, vol. 52, no. 17, pp. 12564–12571, 1995.

## Research Article

# Vapor Sensing Using Conjugated Molecule-Linked Au Nanoparticles in a Silica Matrix

Shawn M. Dirk,<sup>1</sup> Stephen W. Howell,<sup>2</sup> B. Katherine Price,<sup>3</sup> Hongyou Fan,<sup>4</sup> Cody Washburn,<sup>1</sup> David R. Wheeler,<sup>5</sup> James M. Tour,<sup>3</sup> Joshua Whiting,<sup>6</sup> and R. Joseph Simonson<sup>6</sup>

<sup>1</sup>Organic Materials Department, Sandia National Laboratories, MS-0892, Albuquerque, NM 87185, USA

<sup>2</sup>Advanced Sensor Technologies Department, Sandia National Laboratories, MS-0892, Albuquerque, NM 87185, USA

<sup>3</sup>Departments of Chemistry and Mechanical Engineering and Materials Science, The Smalley Institute for Nanoscale Science and Technology, Rice University, MS-222, 6100, Houston, TX 77005, USA

<sup>4</sup>Ceramic Processing and Inorganic Department, Sandia National Laboratories, MS-1349, Albuquerque, NM 87185, USA

<sup>5</sup>Biosensors and Nanomaterials Department, Sandia National Laboratories, MS-0892, Albuquerque, NM 87185, USA

<sup>6</sup>Micro-Total-Analytical Systems Department, Sandia National Laboratories, MS-0892, Albuquerque, NM 87185, USA

Correspondence should be addressed to Shawn M. Dirk, [smdirk@sandia.gov](mailto:smdirk@sandia.gov)

Received 20 June 2008; Accepted 10 October 2008

Recommended by Jose A. Pomposo

Cross-linked assemblies of nanoparticles are of great value as chemiresistor-type sensors. Herein, we report a simple method to fabricate a chemiresistor-type sensor that minimizes the swelling transduction mechanism while optimizing the change in dielectric response. Sensors prepared with this methodology showed enhanced chemoselectivity for phosphonates which are useful surrogates for chemical weapons. Chemoselective sensors were fabricated using an aqueous solution of gold nanoparticles that were then cross-linked in the presence of the silica precursor, tetraethyl orthosilicate with the  $\alpha$ -,  $\omega$ -dithiolate (which is derived from the in situ deprotection of 1,4-di(Phenylethynyl-4',4''-diacetylthio)-benzene (**1**) with wet triethylamine). The cross-linked nanoparticles and silica matrix were drop coated onto interdigitated electrodes having 8  $\mu\text{m}$  spacing. Samples were exposed to a series of analytes including dimethyl methylphosphonate (DMMP), octane, and toluene. A limit of detection was obtained for each analyte. Sensors assembled in this fashion were more sensitive to dimethyl methylphosphonate than to octane by a factor of 1000.

Copyright © 2009 Shawn M. Dirk et al. This is an open access article distributed under the Creative Commons Attribution License, which permits unrestricted use, distribution, and reproduction in any medium, provided the original work is properly cited.

## 1. Introduction

The ability to effectively detect harmful chemical agents, including chemical weapons, is a huge concern in today's world. Numerous types of chemicals can be used as chemical warfare agents, each with widely different structures, making detection of them increasingly difficult. One approach to chemical detection involves the use of sensors comprised of conductive elements including carbon particles [1], carbon nanotubes [2–4], and metal nanoparticles [5–14], each embedded in a nonconductive matrix applied to a set of interdigitated electrodes (IDEs) to provide sensors known as chemiresistors. In the above cases, the nonconductive matrix imparts chemoselectivity. Typically in metal nanoparticle-based chemiresistors, this matrix is the coating on metal nanoparticles.

Chemiresistors may be probed by evaluating the current passing through the sensor as a bias is applied to one of the IDEs. Several publications have described the signal transduction mechanism as an activated tunneling model that contains two terms as shown in the following equation [10, 15, 16]:

$$\sigma = \sigma_0 e^{(-\delta\beta)} e^{(-E_a/RT)}. \quad (1)$$

In this expression,  $\sigma$  is the electronic conductivity of the film,  $\delta$  is the interparticle distance,  $\beta$  is the electronic coupling coefficient (effectively a measure of the density of states (DOS) available between conducting particles),  $E_a$  is the activation energy for electron transfer between adjacent conducting particles,  $R$  is the gas constant, and  $T$  is the absolute temperature. The first exponential factor takes into

account the effect of nanoparticle spacing and the DOS overlaps between nanoparticles, and the second exponential term is related to the permittivity of the film.

In most cases, the analyte affects both factors of the activated tunneling model serving both as a solvent, swelling the nanoparticle/matrix, as well as changing the effective dielectric constant of the sensing film. In the case of low dielectric constant analytes, the first exponential factor dominates, and conductivity decreases. In the case of analytes with high dielectric constants, the second factor dominates, and conductivity increases in the presence of the analyte.

In this article, we report the assembly of amine-capped nanoparticles in the presence of both thiolate cross-linker and silica precursor. This nanoparticle cross-linker silica assembly was then deposited onto interdigitated electrodes and exposed to a series of analyte vapors in varying concentrations. Selectivity is provided by both the cross-linking ligand and the silica matrix surrounding the nanoparticles. The silica precursor was chosen to minimize the contribution of the first exponential factor of the activated tunneling mechanism by effectively fixing the value of  $\delta$ , that is, by creating a relatively rigid matrix which exhibits little swelling. This allows the activated tunneling change upon exposure to be dominated by the second factor in order to increase the sensitivity of the sensor to high dielectric constant ( $k$ ) compounds like dimethyl methylphosphonate DMMP ( $k = 22.3$ ) [17].

## 2. Experimental Details

**2.1. Materials and Methods.** All reactions were carried out under a dry nitrogen atmosphere.  $^1\text{H}$  NMR spectra were obtained on a 400 MHz Bruker (Fremont, Calif, USA) Avance-400. Proton chemical shifts ( $\delta$ ) are reported relative to tetramethylsilane (TMS). UV-vis measurements were performed on a Perkin-Elmer (Waltham, Mass, USA) Lambda 25. Centrifugation was performed using a Fisher (Suwanee, Calif, USA) Scientific Marathon 8 K centrifuge. Hydrogen tetrachloroaurate (p.a.), tetraoctylammonium bromide (98%), cetyl trimethyl ammonium bromide (99+%), 1,4-diiodobenzene (98%), trimethylsilylacetylene (98%), dodecylamine (98%), dichlorodimethylsilane (99%), tetraethyl orthosilicate (98%), and sulfuric acid (reagent grade) were purchased and used as received from Acros. (Geel, Belgium) Sodium borohydride (99%), potassium carbonate (99%), tris(dibenzylideneacetone)dipalladium(0), copper(I) iodide (99.999%), triphenylphosphine (99%), tetrahydrofuran (anhydrous, 99.9%, inhibitor free), 1,2-dichloroethane (99%), and hydrogen peroxide (30% solution in water, ACS Reagent) were purchased and used as received from Aldrich. (Milwaukee, Wis, USA) Toluene (certified ACS), methylene chloride (HPLC grade), chloroform (HPLC grade), carbon disulfide (reagent grade), dimethylacetamide (certified), and hexanes (HPLC grade) were purchased from Fisher (Suwanee, Calif, USA) and used as received. Triethylamine (TEA, reagent grade) was purchased from Fisher (Suwanee, Calif, USA) and vacuum was transferred over calcium hydride prior to use in coupling reactions. 4-Iodobenzenesulphonyl

chloride (95%) was purchased and used as received from Lancaster (Windham, NH, USA).

### 2.2. Preparation of Au Nanoparticles

**2.2.1. Thiol-Capped Au Nanoparticles.** The preparation of the capped gold nanoparticles followed the Brust method [18]. The synthesis of gold nanoparticles involved the transfer of hydrogen tetrachloroaurate (0.35 g, 0.87 mmol) dissolved in water (25 mL) to a solution of tetraoctylammonium bromide (2.19 g, 4.01 mmol) in toluene (80 mL). After the gold salt transferred into the organic phase, the aqueous phase was discarded. Octanethiol (26  $\mu\text{L}$ , 0.15 mmol) was added, and sodium borohydride (0.38 g, 10.0 mmol) in water (25 mL) was added too. The solution turned dark red almost immediately, and after 15 minutes the organic phase was separated and passed through a 0.45  $\mu\text{m}$  Teflon filter. The organic solvent was almost completely removed by rotary evaporation, and the resulting solid material was dissolved in a minimal amount of toluene ( $\sim 3$  mL) followed by precipitation with ethanol. The ethanolic suspension was subjected to centrifugation (2000 rpm for 10 minutes) to collect the nanoparticles after decanting the supernate. The precipitation procedure was repeated, and the nanoparticles were stored at  $-20^\circ\text{C}$ .

**2.2.2. Amine-Capped Au Nanoparticles.** The preparation followed a modified Brust method [18]. The dodecylamine replaced the thiol component. Tetrachloroaurate (112 mg) was dissolved with water (25 mL) and poured into a 500 mL round bottomed flask. Tetraoctylammonium bromide (0.37 g, 0.68 mmol) was dissolved into toluene (25 mL) and added to the round bottom flask with stirring. Once the aqueous layer was clear, a solution of dodecylamine (574 mg in toluene, 25 mL) capping agent was added. A fresh solution of sodium borohydride (165 mg in water, 25 mL) was added, and the color immediately changed to very dark red. The contents were stirred for 1 hour. The layers were separated, and the aqueous layer was discarded. The organic solvent was almost completely removed by rotary evaporation. The solid material was dissolved in a minimal amount of toluene ( $\sim 2$  mL) and then precipitated with ethanol. The suspension was subjected to centrifugation (2000 rpm for 10 minutes) to collect the nanoparticles, and the decanted liquid was discarded. The precipitation procedure was repeated, and the nanoparticles were stored at  $-20^\circ\text{C}$ .

**2.2.3. Transfer of Au Nanoparticles into Water [19].** Au nanoparticles (100  $\mu\text{g}$ ) dissolved in chloroform (3 mL) were added to a 100 mL Erlenmeyer flask. A solution of cetyl trimethyl ammonium bromide (20  $\mu\text{g}$ ) dissolved in water (10 mL) was also added to the Erlenmeyer flask. The two-phase mixture was heated until all the chloroform was removed, and the nanoparticles were transferred to the aqueous phase. The nanoparticles were characterized using TEM after the transfer was complete. The nanoparticles had an average size range of 4–6 nm (radius for several batches).

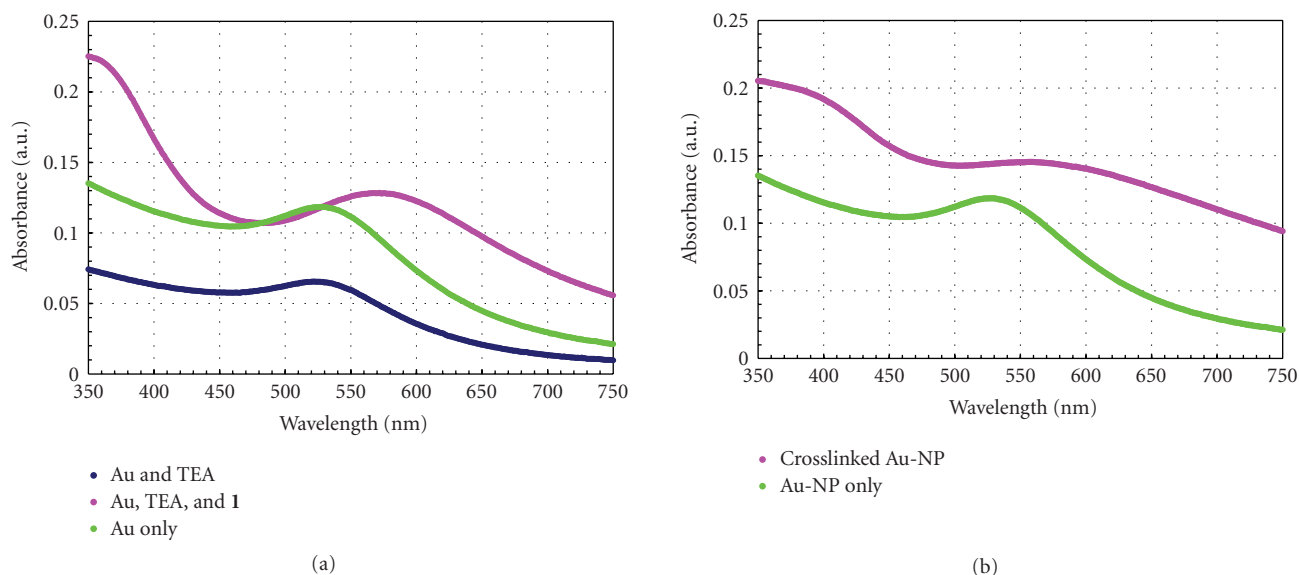


FIGURE 1: UV-vis spectra of (a) alkyl amine capped NPs only and crosslinked, and (b) alkanethiol-capped NPs only and the 1-crosslinked Au-NP. The shifts are 45 and 34 nm, respectively.

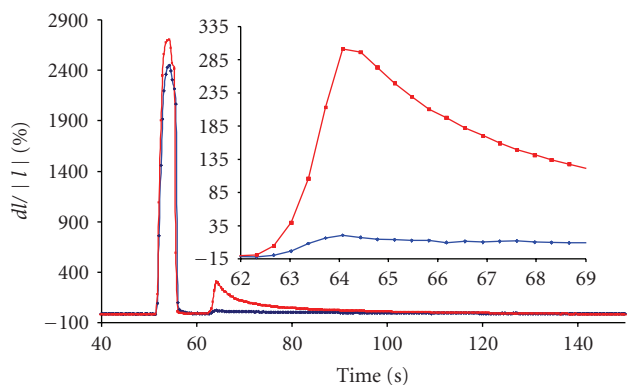


FIGURE 2: 1000 ppm DMMP exposure (1000 ppm max) to TEOS + NP (blue line) and TEOS + PE + NP films (red line). The inset shows an expansion of the DMMP peak.

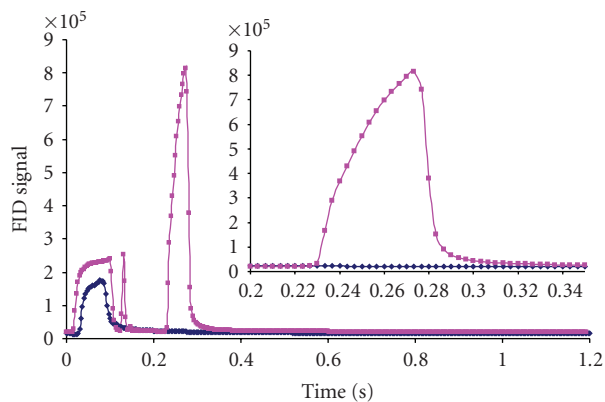


FIGURE 3: The response of the FID detector to a 1000 ppm DMMP in  $\text{CS}_2$  injection with (■), and without a TEOS + NP + PE (◆) film before the FID detector. The inset shows an expansion of the DMMP peak.

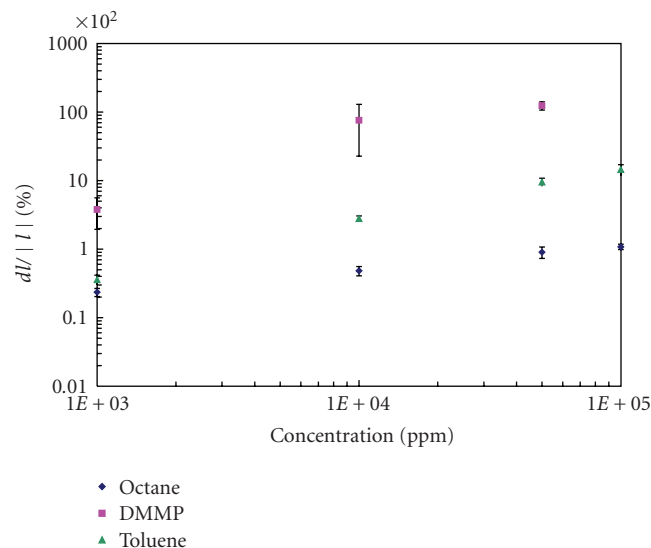


FIGURE 4: Comparison of the response of films consisting of TEOS + PE + NP when exposed to octane (◆), toluene (▲), and DMMP (■). The response of the film is presented as a log/log plot for clarity.

### 2.3. Preparation of Oligophenylene Ethynylene

**2.3.1. General Pd/Cu Coupling Reaction Procedures [20].** All solids, including the aryl halide, alkyne, copper iodide, triphenylphosphine, and palladium catalyst, were added to an oven dried sealed glass tube. The atmosphere was removed via vacuum and replaced with dry argon. THF, remaining liquids, and triethylamine were added during stirring. The reaction was then heated if required. Upon cooling, the reaction mixture was filtered via gravity filtration to remove the solids and then diluted with methylene chloride. The

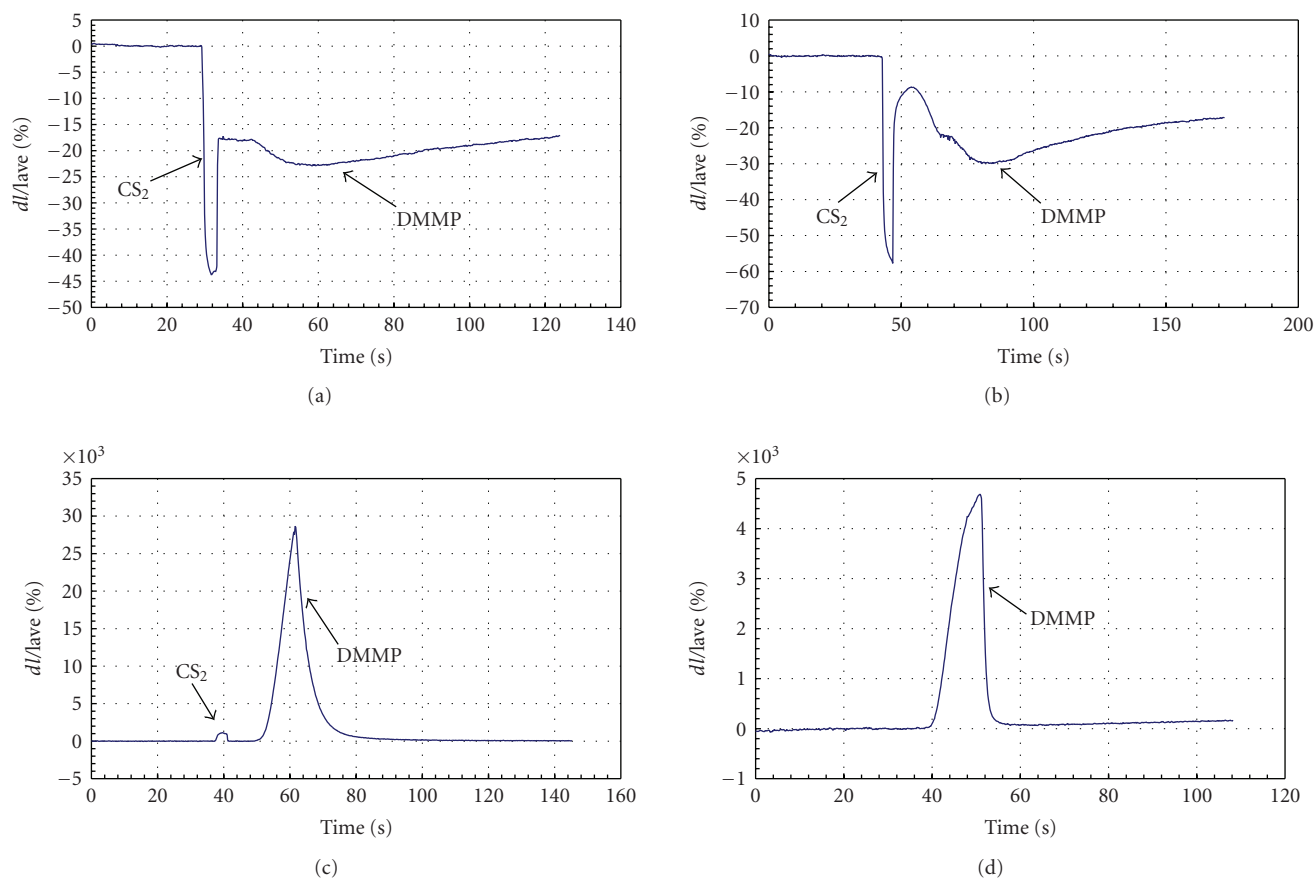


FIGURE 5: Response of gold nanoparticle/10 mL TEOS coated IDEs when exposed to 10 000 ppm DMMP in  $\text{CS}_2$ . The amount of Au nanoparticles was decreased while keeping the TEOS amount fixed. (a) contained 1.25 mg Au NP:10  $\mu\text{L}$  TEOS, (b) contained 0.63 mg Au NP:10  $\mu\text{L}$  TEOS, (c) contained 0.31 mg Au NP:10  $\mu\text{L}$  TEOS, (d) contained 0.16 mg Au NP:10  $\mu\text{L}$  TEOS.

reaction mixture was extracted with aqueous ammonium chloride ( $\times 3$ ). The organic layer was dried with magnesium sulfate and then filtered, and the solvent was removed via rotary evaporation.

**2.3.2. General Procedure for the Deprotection of Trimethylsilyl-Protected Alkynes [21].** The protected alkyne, potassium carbonate (5 equivalents per protected alkyne), methanol, and methylene chloride were added to a round bottom flask equipped with a stir bar. The reaction was stirred at room temperature, and upon completion the reaction mixture was diluted with methylene chloride and washed with brine ( $3\times$ ). The organic layer was dried over anhydrous magnesium sulfate, and the solvent was removed via rotary evaporation.

**2.3.3. Synthesis of 1,4-Bis(Trimethylsilylethynyl)Benzene [22].** Diiodobenzene (3.30 g, 10 mmol), tris(dibenzylideneacetone) dipalladium(0) (0.28 g, 0.30 mmol), copper(I) iodide (0.23 g, 1.20 mmol), triphenylphosphine (0.63 g, 2.40 mmol), trimethylsilyl acetylene (3.2 mL, 22.0 mmol), triethylamine (5.6 mL), and tetrahydrofuran (20 mL) were coupled according to the general coupling procedure above. The crude product was carried directly onto the next synthetic step.

**2.3.4. Synthesis of 1,4-(Diethynyl)Benzene [22].** 1,4-Bis(trimethylsilylethynyl)benzene was deprotected with potassium carbonate (8.3 g, 60.0 mmol), methanol (50 mL), and dichloromethane (50 mL) according to the general deprotection procedure above to yield 1.5 g (100%) of a crystalline pale white solid,  $^1\text{H}$  NMR (400 MHz,  $\text{CDCl}_3$ ) 7.42 (s, 4H), 3.15 (s, 2H).

**2.3.5. Synthesis of S-Acetyl-4-Iodothiophenol [23].** 4-iodobenzenesulphonyl chloride (6.1 g, 20.0 mmol) was added to a 250 mL round bottom flask, and the atmosphere was removed via vacuum and replaced with argon. Zinc powder (4.6 g, 70.0 mmol) was added to a 500 mL three-neck round bottom flask equipped with a stir bar and an addition funnel, and the atmosphere was removed via vacuum and replaced with argon. Dimethylacetamide (5.6 mL, 60.0 mmol) and 1,2-dichloroethane (100 mL) were added to the 250 mL round bottom flask, and the contents were transferred via cannula into the addition funnel. 1,2-dichloroethane (100 mL) and dimethyldichlorosilane were added to the 500 mL three-neck flask (8.5 mL, 70.0 mmol). The contents of the addition funnel were added drop-wise over a period of 30 minutes to the 500 mL flask. After the complete addition, the reaction was heated to  $75^\circ\text{C}$  for 2 hours. The reaction

mixture was cooled to room temperature, and potassium carbonate (1.52 g, 11.0 mmol) and acetyl chloride (5.7 mL, 80.0 mmol) were added to the reaction flask; the contents were stirred overnight. The crude reaction was worked up with brine and extracted with dichloromethane. The organic phase was dried over magnesium sulfate and then filtered, and the solvents were removed via rotary evaporation to yield 5.4 g (97%) of a crystalline white solid,  $^1\text{H}$  NMR (400 MHz,  $\text{CDCl}_3$ ) 7.72 (*dt*,  $J = 8.4$ , 2 Hz, 2H), 7.11 (*dt*,  $J = 8.4$  Hz, 2.4 Hz, 2H) 2.41 (s, 3H).

*Synthesis of 1,4-di(Phenylethynyl-4',4''-Diacetylthio)-Benzene (1) [24].* S-Acetyl-4-iodothiophenol (2.78 g, 10.0 mmol), 1,4(diethynyl)benzene (0.63 g, 5.0 mmol), tris (dibenzylideneacetone)dipalladium(0) (0.14 g, 0.15 mmol), copper iodide (0.11 g, 0.60 mmol), triphenylphosphine (0.31 g, 1.20 mmol), triethylamine (5.6 mL), and tetrahydrofuran (20 mL) were coupled according to the general coupling procedure above. The crude product was purified via column chromatography (1:1 hexanes:dichloromethane) to yield 1.21 g (82%) of a pale brown solid,  $^1\text{H}$  NMR (400 MHz,  $\text{CDCl}_3$ ) 7.61 (m, 8H) 7.46 (*d*,  $J = 8.4$  Hz, 4H) 2.45 (s, 6H).

**2.4. Cross-Linking the Au Nanoparticles.** An aqueous solution of Au nanoparticles (0.5 mL) and **1** (100  $\mu\text{L}$ , 1 mmol in THF) were combined. Triethylamine (5  $\mu\text{L}$ ) was then added, and a color change was evident within 5 minutes. Tetraethyl orthosilicate (TEOS, 10  $\mu\text{L}$ ) was then added and agitated. UV-vis measurements were taken within 5 minutes after the TEA and TEOS additions to confirm cross-linking.

**2.5. Cross-Linked Nanoparticle Film Deposition.** Interdigitated electrode devices were cleaned with acetone (30 seconds bath and rinse) and rinsed with DI water. The device was then submerged in Piranha (1:1 30% hydrogen peroxide and conc. sulfuric acid) for 2 minutes and rinsed with copious amounts of DI water. *Caution: piranha is a very strong oxidizer and reacts violently with organics.* The surface was dried with  $\text{CO}_2$ . Prior to Au nanoparticle/silica deposition, the interdigitated electrode containing substrate was electrically characterized as open using a digital multimeter. The films were produced by flooding the surface with the cross-linked Au nanoparticle/silica solution and allowing the solvent to evaporate. The films that were produced in this manner had reproducible initial resistances. The thickness was measured with atomic force microscopy (AFM).

**2.6. Substrate Exposure to Analytes.** Dimethyl methylphosphonate, toluene, and octane were evaluated as analytes. The analytes are dissolved in 1 mL  $\text{CS}_2$  and injected into a Hewlett Packard 5850 split injection gas chromatograph equipped with 1 meter 100  $\mu\text{m}$  ID capillary column coated with a polydimethylsiloxane stationary phase at ambient temperature. The carrier gas was hydrogen, and the split was 0.33. The flow rate through the column was 28 sccm. The injection port was heated to 250°C. Gas flow exited the capillary column and entered a custom-made test fixture

described below. Gas left the test fixture and returned to the HP FID detector heated to 250°C. The injection volume was 1  $\mu\text{L}$ , and repeated injections were performed with an autoinjection tower for reproducibility.

After the Au nanoparticle/silica assembly, the functionalized substrate was placed in a custom-made silco-coated stainless steel test fixture where the assembled substrate sits in a recessed slot. The lid of the test fixture contained pogo pins that were connected to a Keithley 6487 current preamp voltage source. The lid included a milled channel to allow gas flow over the 8  $\mu\text{m}$  interdigitated electrodes. The lid was sealed with an external O-ring. The voltage source and current measurement instruments were controlled by a custom LabVIEW program. Prior to analyte exposure, an I(V) trace was performed by cycling the voltage from 0 mV to 100 mV to -100 mV to 0 mV in order to determine the resistance of the working sensor device. During an analyte exposure, 100 mV was typically applied to the substrate, and the current was measured.

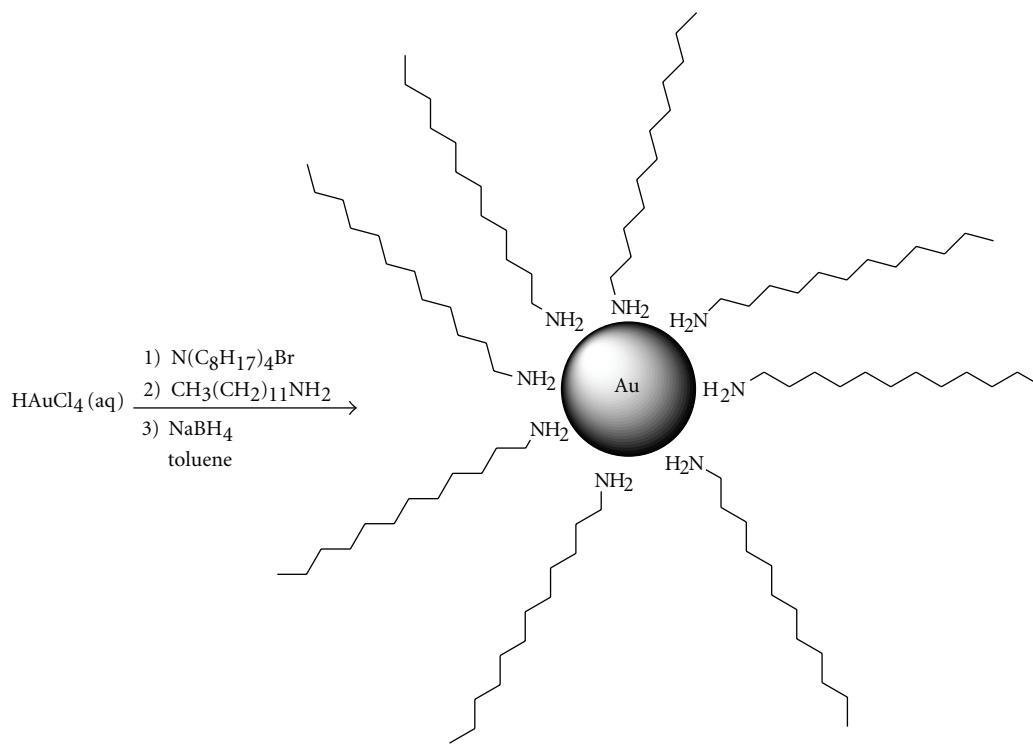
### 3. Results and Discussion

**3.1. Preparation of the Nanoparticle/Silica Film.** Initially Brust-type [18] nanoparticles capped with alkyl thiols were transferred into water by the method of Fan and used to create a nanoparticle film. The strategy employed was to mix the nanoparticles, a silica precursor (tetraethyl orthosilicate), and a cross-linking molecule **1** together in the presence of a reagent to facilitate both the hydrolysis of the tetraethyl orthosilicate and the deprotection of the thioacetate groups as shown in Scheme 1.

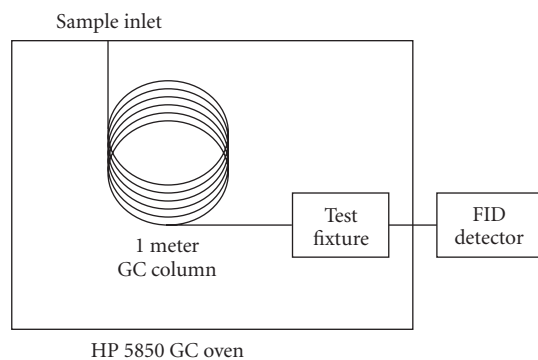
Two common methods used to deprotect thiol acetate groups include  $\text{NH}_4\text{OH}$  in THF [25] and  $\text{H}_2\text{SO}_4$  in  $\text{CH}_2\text{Cl}_2/\text{CH}_3\text{OH}$  [26]. In our case, we were limited to water as the solvent, and attempts to deprotect the thiol acetate groups with these protocols in the presence of the silica precursor tetraethyl orthosilicate and the amine-capped Au nanoparticles proved unsuccessful. Attempted ammonium hydroxide which facilitated deprotection of the thioacetate group resulted in a very fast TEOS condensation rate, and a silica gel resulted within seconds of the base addition. This gellation precluded the desired organic cross-linking of the metal nanoparticles. In the case of the  $\text{H}_2\text{SO}_4$  facilitated deprotection, the rate of condensation of the hydrolyzed tetraethyl orthosilicate was slower than the base-catalyzed case; however, the deprotection of the thioacetate in water was still slower, so that adequate cross-linking or the nanoparticles were again precluded (as determined by NMR).

Sharporenko et al. successfully demonstrated that a thiol acetate group could be deprotected with wet triethylamine in situ to form a self-assembled monolayer [27]. The use of this deprotection method resulted in a useable ratio of the TEOS condensation rate to thiol acetate deprotection rate in the work described here. A color change was apparent within minutes, confirming cross-linking of the Au nanoparticles (NPs) due to the expected change in plasmon resonance. If the solution was allowed to react (cross-link) for several more minutes (~10 minutes), the nanoparticles precipitated from





SCHEME 2: Preparation of alkyl amine gold nanoparticles by a modification of the Brust method [18].



SCHEME 3: The layout of the test structure used to determine analyte selectivity and sensitivity.

broader DMMP peak. The blue trace is the normalized change in signal from an interdigitated electrode that was functionalized with Au nanoparticles and the silica precursor TEOS. The red trace is the normalized change in signal from an interdigitated electrode that was functionalized with Au nanoparticles cross-linked with **1** and the silica precursor TEOS. The **1**-crosslinked nanoparticle-functionalized device was more sensitive to the same concentration of DMMP, as reflected by the eight-fold increase in detector response.

Figure 3 shows the FID response to the same 1000 ppm DMMP injection both with and without the custom-made test fixture in line with the FID. The peak width of the

CS<sub>2</sub> is not dramatically widened with the test fixture in line; however, the DMMP peak appears never to reach the FID detector. This could be evidence of the gettering ability of the assembled film. Based on this evidence, part of the film selectivity to DMMP could arise from the silica matrix surrounding the Au NPs.

The normalized signal response to octane, toluene, and DMMP at various concentrations is shown in Figure 4 and was used to determine the sensitivity of the electrode sensor [13]. Sensitivity is usually defined as the slope of the output signal for a given set of concentrations; as such sensitivity of the assembled sensor was determined for octane (8.0 e<sup>-4</sup>% change/ppm), toluene (1.4 e<sup>-2</sup>% change/ppm), and DMMP (8.0 e<sup>-1</sup>% change/ppm) between the range of 100 ppm and 50 000 ppm.

The limits of detection (LoD) for octane (190 ppm in CS<sub>2</sub>), toluene (80 ppm in CS<sub>2</sub>), and DMMP (60 ppm in CS<sub>2</sub>) were determined from a plot of the log normalized signal change versus log concentration. Based on this plot, a simple extrapolation was used in combination with an arbitrary signal to noise ratio of five (corresponding to 10% noise) to determine the LoD. In practice, these LoD values were not realized in our experiments likely due to a nonoptimized test cell configuration that leads to band broadening and sensitivity loss. No effort was made to reduce the dead volume of the sensor cell.

The nanoparticles used in the sensing matrix had an average radius size of 4–6 nm, and no attempt was made to synthesize nanoparticles of different sizes or of different

metals. Presumably, the electron transport properties of the sensing film could be tailored with modifications of both the metal as well as the size of the nanoparticles and will be the subject of future work.

**3.3. Role of the Au Nanoparticle to Silica Ratio.** Several experiments were performed where the Au nanoparticle to TEOS ratio was modified, and the IDEs were evaluated upon exposure to DMMP, as shown in Figure 5. Experiments with large Au nanoparticle:TEOS ratios show results consistent with a conduction mechanism dominated by the first exponential factor of the activated tunneling model. Accordingly, the conductivity was decreased in the presence of both the DMMP ( $k = 22.3$ ) and the solvent  $\text{CS}_2$  ( $k = 2.6$ ) [28]. Experiments with small Au nanoparticle:TEOS ratios demonstrated results consistent with a conduction mechanism dominated by the second exponential factor of the activated tunneling model, and showed an increase in conductivity for DMMP. The sample prepared with 0.31 mg Au/10 mL TEOS exhibited the most sensitivity to DMMP, whereas the smallest Au nanoparticle:TEOS ratio (0.16 mg Au/10 mL TEOS) was not as sensitive. In the latter case, the sensitivity to DMMP is attributed to slow diffusion of the analyte into the sensing film during this nonequilibrium measurement, due to the highly cross-linked nature of the sensing matrix.

#### 4. Conclusion

Interdigitated electrodes were functionalized by a flood coating technique, using dodecylamine-capped Au nanoparticles cross-linked with a phenylene ethynylene oligomer in a silica matrix. Control of the nanoparticle:TEOS ratio enables control over which factor dominates in the activated tunneling model. Sensors prepared with 0.31 mg Au nanoparticles:10  $\mu\text{L}$  TEOS exhibited the greatest increase in conductance upon exposure to DMMP, whereas sensors prepared with 1.25 mg Au nanoparticles:10  $\mu\text{L}$  TEOS showed decreases in conductivity upon exposure to DMMP. Devices functionalized with 0.31 mg Au nanoparticles:10  $\mu\text{L}$  TEOS were 1000 times more sensitive to DMMP than to octane.

#### Acknowledgments

Sandia is a multiprogram laboratory operated by Sandia Corporation, a Lockheed Martin Company, for the US Department of Energy under Contract DE-AC04-94AL8500. The same Department of Energy contract supported the internship of BKP when working at Sandia, while her work at Rice University was supported by the Defense Advanced Research Projects Agency.

#### References

- [1] T. Gao, M. D. Woodka, B. S. Brunshwig, and N. S. Lewis, "Chemiresistors for array-based vapor sensing using composites of carbon black with low volatility organic molecules," *Chemistry of Materials*, vol. 18, no. 22, pp. 5193–5202, 2006.
- [2] K.-S. Teh and L. Lin, "MEMS sensor material based on polypyrrole-carbon nanotube nanocomposite: film deposition and characterization," *Journal of Micromechanics and Microengineering*, vol. 15, no. 11, pp. 2019–2027, 2005.
- [3] J. K. Abraham, B. Philip, A. Witchurch, V. K. Varadan, and C. C. Reddy, "A compact wireless gas sensor using a carbon nanotube/PMMA thin film chemiresistor," *Smart Materials and Structures*, vol. 13, no. 5, pp. 1045–1049, 2004.
- [4] K. Cattanaach, R. D. Kulkarni, M. Kozlov, and S. K. Manohar, "Flexible carbon nanotube sensors for nerve agent simulants," *Nanotechnology*, vol. 17, no. 16, pp. 4123–4128, 2006.
- [5] C.-Y. Yang, C.-L. Li, and C.-J. Lu, "A vapor selectivity study of microsensor arrays employing various functionalized ligand protected gold nanoclusters," *Analytica Chimica Acta*, vol. 565, no. 1, pp. 17–26, 2006.
- [6] T. Vossmeier, B. Guse, I. Besnard, R. E. Bauer, K. Müllen, and A. Yasuda, "Gold nanoparticle/polyphenylene dendrimer composite films: preparation and vapor-sensing properties," *Advanced Materials*, vol. 14, no. 3, pp. 238–242, 2002.
- [7] P. Pang, J. Guo, S. Wu, and Q. Cai, "Humidity effect on the dithiol-linked gold nanoparticles interfaced chemiresistor sensor for VOCs analysis," *Sensors and Actuators B*, vol. 114, no. 2, pp. 799–803, 2006.
- [8] H. Lei and W. G. Pitt, "Selection of polymeric sensor arrays for quantitative analysis," *Sensors and Actuators B*, vol. 120, no. 2, pp. 386–391, 2007.
- [9] N. Krasteva, I. Besnard, Y. Joseph, R. Krustev, A. Yasuda, and T. Vossmeier, "Analyte sorption and distribution profiles in thin metal nanoparticle/organic composite films-implication to the mechanism of vapor sensing," *Chemical Sensors*, vol. 20, supplement B, pp. 278–279, 2004.
- [10] N. Krasteva, B. Guse, I. Besnard, A. Yasuda, and T. Vossmeier, "Gold nanoparticle/PPI-dendrimer based chemiresistors—vapor-sensing properties as a function of the dendrimer size," *Sensors and Actuators B*, vol. 92, no. 1-2, pp. 137–143, 2003.
- [11] Y. Joseph, B. Guse, A. Yasuda, and T. Vossmeier, "Chemiresistor coatings from Pt- and Au-nanoparticle/nonanedithiol films: sensitivity to gases and solvent vapors," *Sensors and Actuators B*, vol. 98, no. 2-3, pp. 188–195, 2004.
- [12] J. Guo, P. Pang, and Q. Cai, "Effect of trace residual ionic impurities on the response of chemiresistor sensors with dithiol-linked monolayer-protected gold (nano)clusters as sensing interfaces," *Sensors and Actuators B*, vol. 120, no. 2, pp. 521–528, 2007.
- [13] M. E. Franke, T. J. Koplin, and U. Simon, "Metal and metal oxide nanoparticles in chemiresistors: does the nanoscale matter?" *Small*, vol. 2, no. 1, pp. 36–50, 2006.
- [14] N. Cioffi, L. Traversa, N. Ditaranto, et al., "Core-shell Pd nanoparticles embedded in SnOx films. Synthesis, analytical characterisation and perspective application in chemiresistor-type sensing devices," *Microelectronics Journal*, vol. 37, no. 12, pp. 1620–1628, 2006.
- [15] Y. Joseph, N. Krasteva, I. Besnard, et al., "Gold-nanoparticle/organic linker films: self-assembly, electronic and structural characterisation, composition and vapour sensitivity," *Faraday Discussions*, vol. 125, pp. 77–97, 2004.
- [16] W. P. Wuelfing, S. J. Green, J. J. Pietron, D. E. Cliffl, and R. W. Murray, "Electronic conductivity of solid-state, mixed-valent, monolayer-protected Au clusters," *Journal of the American Chemical Society*, vol. 122, no. 46, pp. 11465–11472, 2000.
- [17] H. F. Xiang, H. Y. Xu, Z. Z. Wang, and C. H. Chen, "Dimethyl methylphosphonate (DMMP) as an efficient flame retardant

- additive for the lithium-ion battery electrolytes," *Journal of Power Sources*, vol. 173, no. 1, pp. 562–564, 2007.
- [18] M. Brust, M. Walker, D. Bethell, D. J. Schiffrin, and R. Whyman, "Synthesis of thiol-derivatised gold nanoparticles in a two-phase Liquid–Liquid system," *Journal of the Chemical Society, Chemical Communications*, vol. 7, pp. 801–802, 1994.
- [19] H. Fan, K. Yang, D. M. Boye, et al., "Self-assembly of ordered, robust, three-dimensional gold nanocrystal/silica arrays," *Science*, vol. 304, no. 5670, pp. 567–571, 2004.
- [20] K. Sonogashira, Y. Tohda, and N. Hagihara, "Convenient synthesis of acetylenes: catalytic substitutions of acetylenic hydrogen with bromo alkenes, iodo arenes, and bromopyridines," *Tetrahedron Letters*, vol. 16, no. 50, pp. 4467–4470, 1975.
- [21] C. Cai and A. Vasella, "Oligosaccharide analogues of polysaccharides—part 3. A new protecting group for alkynes: orthogonally protected dialkynes," *Helvetica Chimica Acta*, vol. 78, no. 3, pp. 732–757, 1995.
- [22] G. J. Bodwell, D. O. Miller, and R. J. Vermeij, "Nonplanar aromatic compounds. 6. [2]paracyclo[2](2,7)pyrenophane. A novel strained cyclophane and a first step on the road to a "Vögtle" Belt," *Organic Letters*, vol. 3, no. 13, pp. 2093–2096, 2001.
- [23] J. Wu, C. Chi, X. Wang, J. Li, X. Zhao, and F. Wang, "A one-pot procedure to prepare S-protected 4-iodothiophenols," *Synthetic Communications*, vol. 30, no. 23, pp. 4293–4298, 2000.
- [24] N. Stuhr-Hansen, J. K. Sørensen, K. Moth-Poulsen, J. B. Christensen, T. Bjørnholm, and M. B. Nielsen, "Synthetic protocols and building blocks for molecular electronics," *Tetrahedron*, vol. 61, no. 52, pp. 12288–12295, 2005.
- [25] J. M. Tour, L. Jones II, D. L. Pearson, et al., "Self-assembled monolayers and multilayers of conjugated thiols,  $\alpha,\omega$ -dithiols, and thioacetyl-containing adsorbates. Understanding attachments between potential molecular wires and gold surfaces," *Journal of the American Chemical Society*, vol. 117, no. 37, pp. 9529–9534, 1995.
- [26] L. Cai, Y. Yao, J. Yang, D. W. Price Jr., and J. M. Tour, "Chemical and potential-assisted assembly of thiolacetyl-terminated oligo(phenylene ethynylene)s on gold surfaces," *Chemistry of Materials*, vol. 14, no. 7, pp. 2905–2909, 2002.
- [27] A. Shaporenko, M. Elbing, A. Blaszczyk, C. von Hänisch, M. Mayor, and M. Zharnikov, "Self-assembled monolayers from biphenyldithiol derivatives: optimization of the deprotection procedure and effect of the molecular conformation," *Physical Chemistry B*, vol. 110, no. 9, pp. 4307–4317, 2006.
- [28] M. G. Gaikwad, S. Deuskar, and S. K. David, "Study of dependence of dielectric constant of liquids on free volume," *Solid State Communications*, vol. 39, no. 1, pp. 65–69, 1981.

## Research Article

# Polyamide 66/Brazilian Clay Nanocomposites

E. M. Araújo,<sup>1</sup> K. D. Araujo,<sup>1</sup> R. A. Paz,<sup>1</sup> T. R. Gouveia,<sup>1</sup> R. Barbosa,<sup>1</sup> and E. N. Ito<sup>2</sup>

<sup>1</sup> Department of Materials Engineering, Federal University of Campina Grande, Avenida Aprígio Veloso, 882, Bodocongó, CEP 58429-900, Campina Grande, PB, Brazil

<sup>2</sup> Department of Materials Engineering, Federal University of São Carlos, CEP 13565-905, São Carlos, SP, Brazil

Correspondence should be addressed to E. M. Araújo, edcleide@dema.ufcg.edu.br

Received 7 July 2008; Accepted 10 October 2008

Recommended by Jose A. Pomposo

Polyamide 66 (PA66)/Brazilian clay nanocomposites were produced via direct melt intercalation. A montmorillonite sample from the Brazilian state of Paraíba was organically modified with esthearildimethylammonium chloride (Praepagen), quaternary ammonium salt and has been tested to be used in polymer nanocomposites. The dispersion analysis and the interlayer spacing of the clay particles in matrix were investigated by X-ray diffraction (XRD) and transmission electron microscopy (TEM). Thermal behavior of the obtained systems was investigated by differential scanning calorimetry (DSC), thermogravimetry (TG), and heat deflection temperature (HDT) was reported too. The nanocomposites exhibited a partially exfoliated structure, very interesting HDT values which are higher than those of pure PA66, and good thermal stability.

Copyright © 2009 E. M. Araújo et al. This is an open access article distributed under the Creative Commons Attribution License, which permits unrestricted use, distribution, and reproduction in any medium, provided the original work is properly cited.

## 1. Introduction

Polymer/organoclay nanocomposites present unique properties that are not observed in conventional composites. Incorporation of small amounts of organoclay (<10 wt.%) into polymer matrices may remarkably improve dimension stability, mechanical, thermal, optical, electrical, and gas barrier properties, and decrease the flammability. This happens due to the large contact area between polymer and clay on a nanoscale as reported on literature [1–11]. The incorporation of organoclays into polymer matrices has been known for 50 years and one of the pioneering works was from Toyota as reported by Cho and Paul [2]. To be compatible with polymer matrices, sodium smectite clays need to be modified by using quaternary ammonium salts with at least 12 carbon atoms in aqueous dispersions. In these dispersions, the clay particles or layers must be separated one from another and not be stacked in order to facilitate the introduction of the organic compounds. As a result, the clay exchangeable cations are replaced by the organic cations of the quaternary ammonium salt that are adsorbed on the negative sites of the clay surfaces. The obtained clay is known as organoclay [7–12]. Polyamide 66 (PA66) is an important engineering plastic, but PA66 matrix nanocomposites have been little investigated by researchers up to now [13–15].

The purpose of this paper is to analyze the effect of the Brazilian clay incorporation on the thermal behavior and morphology of Polyamide 66/clay nanocomposites.

## 2. Experimental

**2.1. Materials.** Polyamide 66 (PA66, Technyl A216, São Paulo/SP, Brazil) was supplied by Rhodia/Brazil and used; as a composite matrix. Na-montmorillonite (MMT, Brasgel PA, Boa Vista/PB, Northeast of Brazil) supplied by Bentonit União do Nordeste with a cation exchange capacity (CEC) of 90 meq/100 g, and interlayer spacing  $d_{001} = 12.5 \text{ \AA}$  was used as nanofiller. The quaternary ammonium salt esthearildimethylammonium chloride—Praepagen (P) with industrial grade, supplied by Clariant/Brazil, was used (as soon as it was received) for MMT clay modification.

**2.2. Preparation of Organoclays.** The Na-MMT clay was modified organically (named as organoclay) with quaternary ammonium salt according to the procedure described by Barbosa [4] and Araújo et al. [7–12, 16].

**2.3. Preparation of Nanocomposites.** PA66/unmodified clay (MMT) as well as PA66/modified clay (organoclay-OMMT)

nanocomposites, containing 2 wt.% of clay, were melt compounded in a counterrotating twin-screw extruder (attached to a Haake System 90 Torque Rheometer) operating at 270–280°C and 40 rpm. Samples for tensile tests (ASTM D638) were injection molded in a Fluidmec machine at 280°C. Before each processing, the PA66 pellets were dried under vacuum at 80°C for 24 hours. The rheological characterization of the nanocomposites containing 2 wt.% of clay was carried out in an intensive batch mixer Rheomix 600 equipped with roller blades attached to a Haake System 90, operating at 280°C, 60 rpm, and 10 minutes. The clays were added to PA66, after 2.5 minutes.

**2.4. Characterization of Dispersibility of the Clay in Polymer Matrix.** The structure of PA66/MMT and PA66/OMMT composites was characterized by X-ray diffraction (XRD) and transmission electron microscopy (TEM). XRD measurement was performed using an XRD-6000 Shimadzu diffractometer (40 kV, 30 mA) with  $2\theta$  scan range of 2–30° at room temperature, at a scanning speed of 2°/min with Cu ( $\lambda = 0.154$  nm). TEM analysis was carried out in a Philips CM120 Equipment with 120 kV. Samples were cryogenically microtomed into ultrathin sections (25–50 nm thick) with a diamond knife using an RMC MT-7000 under cryogenic conditions (−80°C) inside the microtoming chamber.

**2.5. Differential Scanning Calorimetry (DSC).** DSC analyses were carried out using a Shimadzu DSC-50 differential scanning calorimeter thermal analyzer. About 10 mg of the polymer sample was weighed very accurately in the aluminum DSC pan and placed in the DSC cell. It was heated from 30 to 300°C at a rate of 20°C/min under nitrogen atmosphere. The sample was kept for 5 minutes at this temperature to eliminate the heat history. The  $\Delta H_{mo}$  values for PA66 matrix were taken as 195.9 J/g [14].

**2.6. Thermogravimetry (TG).** The thermal stability was measured by thermogravimetry using a Shimadzu TGA-51 equipment, with a heating ramp of 20°C/min in nitrogen and air atmospheres from 20 to 900°C.

**2.7. Heat Deflection Temperature (HDT).** Heat deflection temperature (HDT) was obtained in a Davenport equipment, 09z64, with 1800 kPa, according to ASTM D648. The samples were immersed in a silicon oil bath at a rate of 120°C/h.

### 3. Results and Discussion

**3.1. Structure of PA66/Clay Nanocomposites.** Figure 1 presents the X-ray diffraction patterns for the PA66 systems with 2 wt.% of unmodified (MMT) and modified clay (OMMT). The interlayer distance was determined by the diffraction peak in the X-ray method, using the Bragg equation. It can be observed for the modified clay (OMMT) three peaks corresponding to an interlayer spacing  $d_{001}$  of 29.2, 19.2, and 12.5 Å. The two first peaks indicate that the intercalation of the salt between the layers of clay has occurred. Another

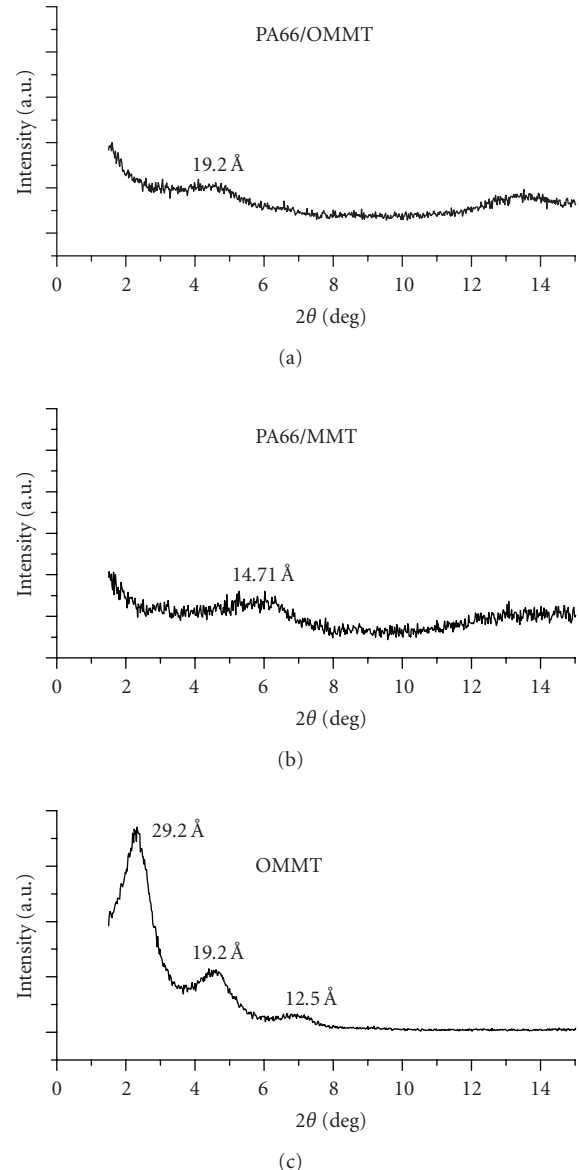


FIGURE 1: XRD patterns of montmorillonite clay modified with Praepagen salt (OMMT), PA66/MMT, and PA66/OMMT nanocomposites.

peak corresponding to interlayer spacings of 12.5 Å ( $d_{001}$  for unmodified clay-MMT) is probably due to an incomplete ion exchange, with some residual Na-MMT remaining in the material, according to the literature [7, 8]. The results indicated that the quaternary ammonium salt was intercalated between two basal planes of MMT, leading to an expansion of the interlayer spacing. It can be observed too for PA66/MMT system a diffraction peak around 14.71 Å, which is close to the distance of 12.5 Å of the unmodified clay, indicating that the increase of the basal spacing practically did not occur. On the other hand, the sample of the nanocomposite of PA66 with the modified clay (OMMT) presented the displacement of the XRD peak toward a lower angle values, what represents an increase to 19.20 Å in the basal spacing. It can be thus

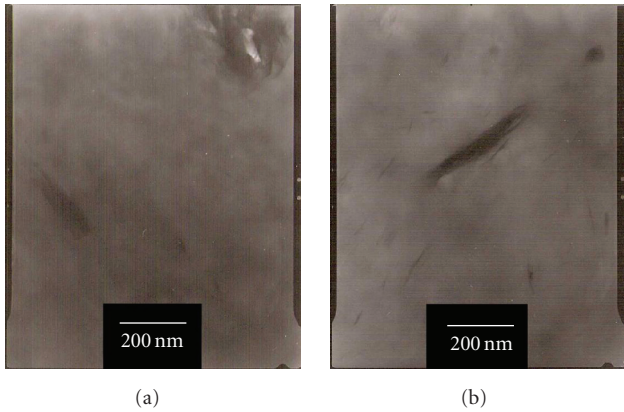


FIGURE 2: TEM photomicrographs of (a) PA66/MMT and (b) PA66/OMMT nanocomposites.

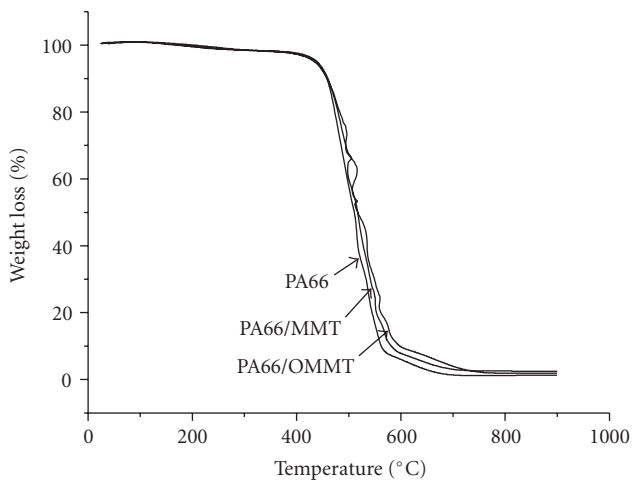


FIGURE 3: TG curves of PA66 and its nanocomposites in nitrogen atmosphere.

noticed that with the organoclay presence, the peak related to the PA66/unmodified clay interlayer spacing disappeared, and a new broad diffraction peak appeared. This peak can be due to the intercalation/partially exfoliation of the polymer chains between the layers of organoclay. These results will be confirmed by TEM.

Figure 2 shows the TEM images of the PA66 systems. In Figure 2(a), it can be seen clearly agglomerates of clay and in Figure 2(b) exists intercalated clay layers but it can be seen too several exfoliated clay layers present in the PA66 matrix. Therefore, the obtained PA66/OMMT systems are partially exfoliated nanocomposites according to the XRD pattern (Figure 1) and the literature [2, 3, 5, 13–15].

**3.2. Thermal Behavior.** Table 1 shows the melting and crystallization parameters of the pure PA66 and its mixtures obtained by DSC, respectively. It can be seen that there was no significant change in the melting and crystallization temperatures of the mixtures. On the other hand, it seems that the presence of the clay improved the heat of fusion,

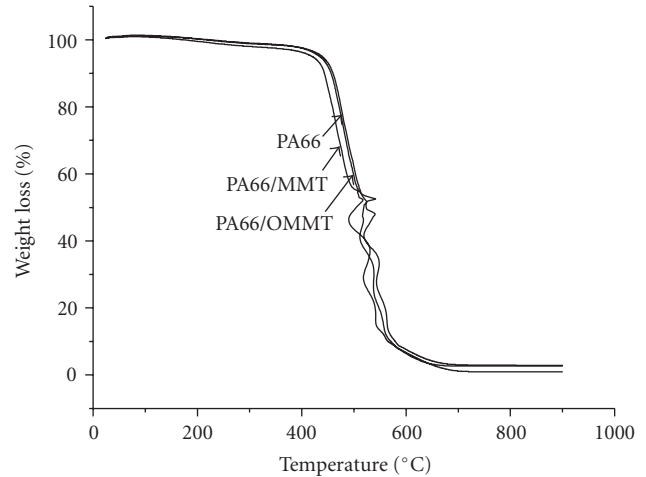


FIGURE 4: TG curves of PA66 and its nanocomposites in air atmosphere.

TABLE 1: Melting and crystallization parameters for PA66 and its nanocomposites.  $T_m$ : melting temperature taken at the melt peak;  $T_c$ : crystallization temperature taken at the crystallization peak;  $\Delta H_m$ : heat of fusion due to PA66 melting, measured through the melting peak;  $X_c$ : degree of crystallinity, taken from  $\Delta H_m/\Delta H_{mo}$ ;  $\Delta H_{mo}$ : heat of fusion for PA66, 100% crystalline, 195.9 J/g [14].

Materials	Heating		Cooling	
	$T_m$ (°C)	$\Delta H_m$ (J/g)	$T_c$ (°C)	$X_c$ (%)
PA66	266.98	50.07	223.45	25.55
PA66/MMT	263.82	60.43	224.74	30.23
PA66/OMMT	263.67	60.80	223.11	30.41

which led to higher crystallinity degree. Probably, the clay acts as nucleation agent in the matrix.

In order to investigate the effect of the organoclay on the thermal stability of PA66/clay nanocomposite, the TG analysis of the systems is presented. The thermal stability of PA66/clay nanocomposites is a little improved with the presence of the organoclay in nitrogen atmosphere, as pointed out in Figure 3. Pure PA66 degrades a little faster than PA66/clay nanocomposites, that is, the nanocomposites are stable up to  $\sim 400^\circ\text{C}$ . Figure 4 shows TG curves using air atmosphere. In these conditions, it can be seen that the nanocomposite containing organoclay presents thermal stability a little superior than PA66/MMT. This suggests that at the range of the used processing temperatures, the degradation of the system did not occur. Apparently, the organoclay has two opposing functions in the thermal stability of the nanocomposites, one is due to barrier property to the oxygen and the other is due to the catalysis effect toward the degradation of the polymer, but the barrier effect is predominant with the addition of low fraction of clay to the polymer matrix, as observed in this work. Only with increasing loading, the catalyzing effect rapidly rises and becomes dominant and the thermal stability of the nanocomposites decreases, according to Araújo et al. [8] and Zhao et al. [17].

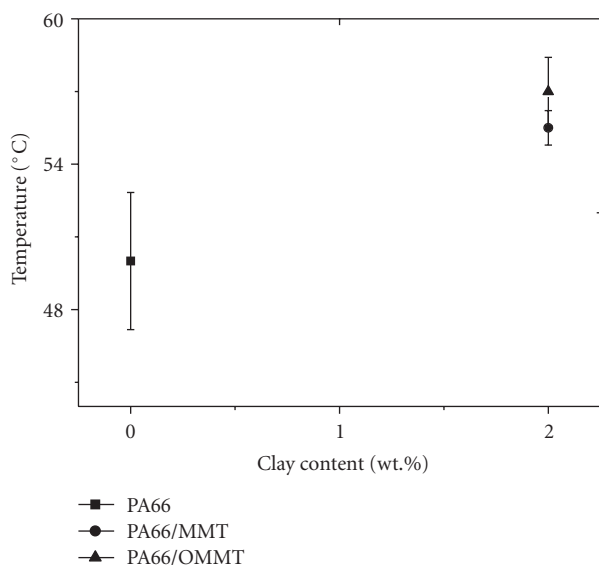


FIGURE 5: Heat deflection temperature of PA66 and its nanocomposites.

**3.3. Heat Deflection Temperature (HDT).** The heat deflection temperature (HDT) can be used to simulate the polymer application in temperatures above the environment temperature and to evaluate the compatibility of the polymer systems. Figure 5 shows the obtained data for HDT of the nanocomposites and pure PA66. The HDT of the pure PA66 stayed in the range of 50°C and for nanocomposites in the range of 56°C. Of the point of view technologic, these values are very interesting since the literature in general mentions that the formation of nanoparticles increases the HDT, the rigidity of the system, and the barrier properties. The presence of organoclay in the PA66 matrix increased the HDT compared to pure PA66.

## 4. Conclusions

Polyamide 66/Brazilian clay nanocomposites were produced via direct melt intercalation. The obtained PA66/organoclay nanocomposites presented partially exfoliated structure. XRD analysis showed that the salt was intercalated between two basal planes of montmorillonite clay. Incorporation of the organoclay improved the thermal stability of PA66. As expected, HDT's properties presented very interesting values for the nanocomposites and larger ones for matrix. This also indicates that the Brazilian clay can be used as a nanoparticle in PA66 nanocomposites.

## Acknowledgments

The authors thank Rhodia, Bentonit União Nordeste, Clarisant, all Brazilian industries, Renami (Rede de Nanotecnologia Molecular e de Interfaces), CTPETRO/MCT/CNPq and MCT/CNPq/Universal for financial support, MSc. Pankaj Agrawal/UFCG/Brazil and Doutorado em Engenharia de Processos/UFCG/Brazil.

## References

- [1] S. A. Body, M. M. Mortland, and C. T. Chiou, "Sorption characteristics of organic compounds on hexadecyltrimethyl ammonium-smectite," *Soil Science Society of America Journal*, vol. 52, pp. 652–657, 1988.
- [2] J. W. Cho and D. R. Paul, "Nylon 6 nanocomposites by melt compounding," *Polymer*, vol. 42, no. 3, pp. 1083–1094, 2001.
- [3] M. Zanetti and L. Costa, "Preparation and combustion behaviour of polymer/layered silicate nanocomposites based upon PE and EVA," *Polymer*, vol. 45, no. 13, pp. 4367–4373, 2004.
- [4] R. Barbosa, *Effect of quaternary ammonium salts in the natural bentonite clay organophilization for the development of HDPE nanocomposites*, M.S. thesis, University of Campina Grande, Campina Grande, Brazil, 2005.
- [5] S. Wang, Y. Hu, Q. Zhongkai, Z. Wang, Z. Chen, and W. Fan, "Preparation and flammability properties of polyethylene/clay nanocomposites by melt intercalation method from Na<sup>+</sup> montmorillonite," *Materials Letters*, vol. 57, no. 18, pp. 2675–2678, 2003.
- [6] C. Zilg, P. Reichert, F. Dietsche, T. Engelardt, and R. Mülhaupt, "Pesquisadores desenvolvem nanocompósitos que atuam como cargas com diferentes finalidades," *Plástico Industrial*, pp. 64–74, February 2000.
- [7] R. Barbosa, E. M. Araújo, T. J. A. Melo, and E. N. Ito, "Comparison of flammability behavior of polyethylene/Brazilian clay nanocomposites and polyethylene/flame retardants," *Materials Letters*, vol. 61, no. 11–12, pp. 2575–2578, 2007.
- [8] E. M. Araújo, R. Barbosa, A. W. B. Rodrigues, T. J. A. Melo, and E. N. Ito, "Processing and characterization of polyethylene/Brazilian clay nanocomposites," *Materials Science and Engineering A*, vol. 445–446, pp. 141–147, 2007.
- [9] E. M. Araújo, R. Barbosa, A. D. Oliveira, C. R. S. Morais, T. J. A. deMelo, and A. G. Souza, "Thermal and mechanical properties of PE/organoclay nanocomposites," *Journal of Thermal Analysis and Calorimetry*, vol. 87, no. 3, pp. 811–814, 2007.
- [10] E. M. Araújo, K. D. Araujo, and T. R. Gouveia, "Physical properties of nylon 66/organoclay nanocomposites," *Materials Science Forum*, vol. 530–531, pp. 702–708, 2006.
- [11] E. M. Araújo, T. J. A. Mélo, L. N. L. Santana, et al., "The influence of organo-bentonite clay on the processing and mechanical properties of nylon 6 and polystyrene composites," *Materials Science and Engineering B*, vol. 112, no. 2–3, pp. 175–178, 2004.
- [12] E. M. Araújo, R. Barbosa, C. R. S. Morais, L. E. B. Soledade, A. G. Souza, and M. Q. Vieira, "Effects of organoclays on the thermal processing of pe/clay nanocomposites," *Journal of Thermal Analysis and Calorimetry*, vol. 90, no. 3, pp. 841–848, 2007.
- [13] H. Qin, Q. Su, S. Zhang, B. Zhao, and M. Yang, "Thermal stability and flammability of polyamide 66/montmorillonite nanocomposites," *Polymer*, vol. 44, no. 24, pp. 7533–7538, 2003.
- [14] F. Chavarria and D. R. Paul, "Comparison of nanocomposites based on nylon 6 and nylon 66," *Polymer*, vol. 45, no. 25, pp. 8501–8515, 2004.
- [15] X. Liu, Q. Wu, and L. A. Berglund, "Polymorphism in polyamide 66/clay nanocomposites," *Polymer*, vol. 43, no. 18, pp. 4967–4972, 2002.

- [16] R. Barbosa, E. M. Araújo, T. J. A. Melo, E. N. Ito, and E. Hage Jr., "Influence of clay incorporation on the physical properties of polyethylene/Brazilian clay nanocomposites," *Journal of Nanoscience and Nanotechnology*, vol. 8, no. 4, pp. 1937–1941, 2008.
- [17] C. Zhao, H. Qin, F. Gong, M. Feng, S. Zhang, and M. Yang, "Mechanical, thermal and flammability properties of polyethylene/clay nanocomposites," *Polymer Degradation and Stability*, vol. 87, no. 1, pp. 183–189, 2005.